

A Critical Review of Thermal Issues in Lithium-Ion Batteries

To cite this article: Todd M. Bandhauer *et al* 2011 *J. Electrochem. Soc.* **158** R1

View the [article online](#) for updates and enhancements.

Discover the EL-CELL potentiostats

- Fully independent test channels with Pstat / GStat / EIS
- Optionally with integrated temperature controlled cell chamber
- Unique Connection Matrix: Switch between full-cell and half-cell control at runtime

www.el-cell.com +49 (0) 40 79012 734 sales@el-cell.com





CRITICAL REVIEWS

in Electrochemical and Solid-State Science and Technology

A Critical Review of Thermal Issues in Lithium-Ion Batteries

Todd M. Bandhauer,^{a,*} Srinivas Garimella,^{a,z} and Thomas F. Fuller^{b,**}

^aSustainable Thermal Systems Laboratory, GWW School of Mechanical Engineering, Georgia Institute of Technology, Atlanta, Georgia 30332, USA

^bCenter for Innovative Fuel Cell and Battery Technologies, Georgia Tech Research Institute and School of Chemical and Biomolecular Engineering, Georgia Institute of Technology, Atlanta, Georgia 30332, USA

Lithium-ion batteries are well-suited for fully electric and hybrid electric vehicles due to their high specific energy and energy density relative to other rechargeable cell chemistries. However, these batteries have not been widely deployed commercially in these vehicles yet due to safety, cost, and poor low temperature performance, which are all challenges related to battery thermal management. In this paper, a critical review of the available literature on the major thermal issues for lithium-ion batteries is presented. Specific attention is paid to the effects of temperature and thermal management on capacity/power fade, thermal runaway, and pack electrical imbalance and to the performance of lithium-ion cells at cold temperatures. Furthermore, insights gained from previous experimental and modeling investigations are elucidated. These include the need for more accurate heat generation measurements, improved modeling of the heat generation rate, and clarity in the relative magnitudes of the various thermal effects observed at high charge and discharge rates seen in electric vehicle applications. From an analysis of the literature, the requirements for lithium-ion thermal management systems for optimal performance in these applications are suggested, and it is clear that no existing thermal management strategy or technology meets all these requirements.

© 2011 The Electrochemical Society. [DOI: 10.1149/1.3515880] All rights reserved.

Manuscript submitted June 24, 2009; revised manuscript received October 2, 2010. Published January 25, 2011.

This article was reviewed by Karen Thomas-Alyea (kethomas@alummi.princeton.edu) and Kandler Smith (kandler.smith@gmail.com).

Electric and hybrid electric vehicles (EV and HEV) may present the best near-term solution for the transportation sector to reduce our dependence on petroleum and to reduce emissions of greenhouse gases and criteria pollutants. Rechargeable lithium-ion batteries are well-suited for these vehicles because they have, among other things, high specific energy and energy density relative to other cell chemistries. For example, practical nickel-metal hydride (NiMH) batteries, which have dominated the HEV market, have a nominal specific energy and energy density of 75 Wh/kg and 240 Wh/L, respectively. In contrast, lithium-ion batteries can achieve 150 Wh/kg and 400 Wh/L,¹ i.e., nearly 2 times the specific energy and energy density.

Whereas lithium-ion batteries are rapidly displacing NiMH and nickel-cadmium secondary batteries for portable and hand-held devices, they have not yet been widely introduced in automotive products. The main barriers to the deployment of large fleets of vehicles on public roads equipped with lithium-ion batteries continue to be safety, cost (related to cycle and calendar life), and low temperature performance²—all challenges that are coupled to thermal effects in the battery. Since the recent introduction of HEV fleets, the industry trend is toward larger batteries required for plug-in hybrids, extended-range hybrids, and all-electric vehicles. These larger battery designs impose greater pressure to lower costs and improve safety.

Furthermore, most of the research on these types of batteries has been related to finding the best material for the electrodes in terms of specific energy, power, and cycle life, but with relatively little attention paid to thermal management.³ This presents a significant

gap in the knowledge commercial manufacturers and developers need to design and fabricate safe, reliable battery systems for EVs and HEVs. Nelson et al.⁴ have suggested that even the long-term technical goals and requirements for HEV batteries determined by the U.S. Department of Energy (USDOE) FreedomCAR and Vehicle Technologies Program (see Table I) imply requirements for effective thermal management of the battery.⁵ For example, because capacity/power degradation accelerates at elevated temperatures,⁶ the goal of 15 year calendar life may imply strict temperature control, even during standby. This further emphasizes the need for a good understanding of lithium-ion battery thermal issues.

In this paper, a critical review of the available literature on the major thermal issues is presented. Specific attention is paid to how temperature and thermal management affect capacity/power fade, thermal runaway, and pack electrical imbalance. Cold temperature performance of lithium-ion cells is also reviewed. Some investiga-

Table I. Summary of FreedomCAR energy storage goals.⁵

Characteristics	Units	Requirements	
		Minimum	Maximum
Peak discharge pulse power (10 s)	kW	25	40
Peak regenerative pulse power (10 s)	kW	20	35
Total available energy (over DOD range where pulse power goals are met)	kWh	300	500
Cold cranking power at -30°C	kW	5	7
Calendar life	years		15
Maximum weight	kg	40	60
Maximum volume	L	32	45
Operation temperature range	°C	-30 to 52	
Survival temperature range	°C	-46 to 66	

* Electrochemical Society Student Member.

** Electrochemical Society Fellow.

^z E-mail: sgarimella@gatech.edu

Table II. Summary of reviewed capacity fade high temperature cycling studies.

Author	Materials	DOD range	Cycle rate	Number of cycles	Test temperature	Capacity fade	Power fade	Key conclusions
Ramadass et al. ^{12,13}	C/LiCoO ₂	4.2–2.0 V	C/1.8	500	25°C 50°C	22.5% 70.6%		Degradation of negative electrode dominated capacity loss
Ehrlich ¹⁴	C/LiCoO ₂	4.2–2.5 V	C/1	500	21°C 45°C	9.0% 13.0%		
	C/LiMn ₂ O ₄	4.2–2.5 V	C/1	500	21°C 45°C	28.0% 51.0%		
Amine et al. ¹⁵	MCMB/LiFePO ₄ (LiPF ₆ electrolyte)	3.8–2.7 V	C/3	100	37°C 55°C	40.0% 70.0%		Dissolution of Fe ²⁺ ions high for both coated and uncoated positive electrodes; high temperature capacity fade can be reduced by selecting appropriate electrolyte
	MCMB/LiFePO ₄ (carbon-coated positive electrode)			50	37°C	40.0%		
	MCMB/LiFePO ₄ (LiBOB electrolyte)			100	37°C	20.0%		
Liu et al. ¹⁶	C/LiFePO ₄	90% DOD	C/2	2628	15°C	7.5%		Capacity fade was primarily due to loss of lithium from repair of SEI on negative electrode; saw no evidence of Fe dissolution in the electrolyte
		50% DOD	6C	757 1376	60°C 45°C	20.1% 22.1%		
Takei et al. ¹⁷	C/LiCoO ₂	3.1–2.5 V 4.2–3.6 V	Unknown	1500 1300	Unknown	0.0% 40.0%		Capacity fade is a strong function of maximum voltage, especially about 3.92 V
Choi and Lim ¹⁸	C/LiCoO ₂	4.2–2.75 V 4.2–3.2 V 4.2–3.3 V 4.2–3.4 V 4.2–3.5 V 4.2–3.55 V	C/1	500	25°C	13.4% 15.5% 17.0% 15.1% 16.1% 15.8%		No appreciable difference in capacity fade due to increasing DOD
Belt et al. ¹⁹	Unknown	75–75% 75–55% 75–35%	Modified 100 Wh profile	120,000	25°C	7.0% 6.2% 7.1%	15.0% 27.0% 43.0%	Capacity fade is not a strong function of DOD, but power fade is a function of DOD—due to positive electrode breakage
Belt et al. ²⁰	Proprietary	25 Wh	PNGV cycle-life test protocol	300,000	30°C 40°C 50°C	15.3% 13.7% 11.7%	15.0% 14.5% 16.1%	Capacity/power fade appears to be independent of temperature for small DOD changes for 75% average SOC

Table III. Summary of reviewed capacity and power fade high temperature storage studies.

Author	Materials	Electrolyte	Soak time	Soak temperature	Soak SOC	Capacity fade	Power fade	Key conclusions
Thomas et al. ⁶	C/LiNi _{0.8} Co _{0.15} Al _{0.5} O ₂		35 weeks	25°C	60%		20%	Power fade is primarily temperature dependent in the first 4 weeks, and both time and temperature dependent thereafter
			20 weeks	55°C	100%		55%	
			4 weeks	25°C	60%		3%	
				35°C			3%	
				45°C			7%	
Smart et al. ²¹	C/Li _{1-x} Ni _y Co _{1-y} O ₂	Medium EC electrolyte	10 days	55°C	100%	14%		Capacity fade at high temperatures is strongly dependent on the EC content—more EC results in less capacity fade; capacity fade is more rapid at higher temperatures
		Low EC electrolyte				35%		
		High EC electrolyte	40 days	55°C for 10 days	100%	11%		
				60°C for 10 days				
				65°C for 10 days				
				70°C for 10 days				

tors have presented thermal models for lithium-ion batteries, which are crucial for predicting their performance in application. Because understanding battery heat generation is fundamentally important for understanding thermal issues, the major investigations in this area are also critically reviewed and gaps in understanding are identified. As a result, the requirements for lithium-ion thermal management systems for optimal performance in HEV and EV applications are identified and discussed. Finally, this leads to recognition of critical gaps in lithium-ion battery thermal management research, which are not filled by current thermal management strategies.

Thermal Effects in Lithium-Ion Batteries

The performance, life, and safety of lithium-ion batteries are all affected by their operation and/or storage temperatures. In this section, a brief overview of the major thermal issues that necessitate thermal management of lithium-ion batteries is presented. These include capacity/power fade, thermal runaway, electrical imbalance among multiple cells in a battery pack, and low temperature performance. Emphasis is placed on the impact of temperature on each of these phenomena. Furthermore, coupling between electrochemical reactions and transport phenomena, which in turn affects the temperature, is discussed. Studies in each area are highlighted and discussed so that critical research gaps in thermal management strategies can be identified.

Capacity/power fade.—The performance degradation of lithium-ion batteries can be characterized by the loss of either available energy (i.e., capacity) or power.⁷ Available energy is lost when the active material inside the battery has been transformed into inactive phases, which reduces capacity at any discharge rate. Power (i.e., rate capability) is reduced when the cell internal impedance increases, which reduces the operating voltage at each discharge rate. The underlying aging mechanisms for these batteries have been examined and summarized in several review documents.^{8–11} Due to the overwhelming number of electrode material and electrolyte solvent/salt combinations used in both commercial batteries and academic studies, it is difficult to develop a coherent and comprehensive picture of all the relevant capacity/power fade mechanisms. However, it is clear that temperature does have an influence on the performance degradation of lithium-ion batteries, and this is true for nearly all positive electrode and electrolyte chemistries. A few of these studies are highlighted in Tables II and III for high temperature cycling and storage, respectively, documenting both power and capacity fade for a variety of positive electrode materials.

In some degradation studies, the battery is repeatedly cycled at a constant rate while the battery is maintained at high temperatures. The data presented by Ramadass et al.,^{12,13} Ehrlich,¹⁴ and Amine et al.¹⁵ are on batteries cycled repeatedly between 100 and 0% state of charge (SOC). In general, the mechanisms for cell degradation depend upon cell chemistry. What is more, as shown in Table II, the

capacity appears to degrade if the battery temperature increases beyond ~50°C regardless of discharge rate or cell chemistry.

Complete charging and discharging is not observed in HEV applications, which typically operate in a charge sustaining mode where the SOC varies over a narrow range. This impact of the SOC range can be observed in the remaining studies listed in Table II. For example, Takei et al.¹⁷ cycled C/LiCoO₂ cylindrical batteries in 25% depth of discharge (DOD) increments, with maximum voltage ranging from 4.27 to 2.78 V. Their results show that the capacity fade increased as the maximum cell voltage increased. In addition, Choi and Lim¹⁸ showed no appreciable difference in capacity fade from changing only the discharge cutoff voltage. This may help explain why the data collected by Belt and co-workers^{19,20} showed no appreciable difference due to temperature in capacity or power fade when cycled at a lower DOD from a lower initial SOC. Because predicting and improving life is essential for meeting cost targets for lithium-ion batteries in HEV applications, additional investigation on how decreased SOC range impacts capacity/power fade at elevated temperatures is warranted.

Capacity and power fade can happen even when the batteries are stored and not cycled, and Table III shows results from two example studies. In the study by Thomas et al.,⁶ the power fade increases substantially when the battery is soaked at a higher SOC and temperature. In addition, their results showed that the power fade in the first 4 week period appeared to be a strong function of temperature, with a significant increase beyond 45°C. Smart et al.²¹ experimentally determined the irreversible capacity loss on a fully charged mesocarbon microbead (MCMB)/Li_{1-x}Ni_yCo_{1-y}O₂ cell to determine the impact on capacity fade from using different electrolytes. They used fully charged cells at high temperatures so that the capacity fade was accelerated. Sample results for a number of solvent mixtures show that the ethylene carbonate (EC) content made a significant impact on capacity fade, with increased concentrations reducing capacity fade. However, it can be seen that for even high EC concentration levels, capacity fade still exists after storing the battery between 55 and 70°C for only 40 days. Clearly, both storage SOC and temperature are critical parameters causing capacity and power reduction even when the battery is not cycled.

Self-discharge.—The studies discussed above all investigated the amount of recoverable energy after storing or cycling lithium-ion batteries at a variety of temperatures. However, batteries can reversibly self-discharge, thus lowering the capacity retained. For example, as explained by Aurbach,²² fully charged graphite electrodes are strong reducing agents and the solid electrolyte interphase (SEI) formed on the surface does not completely passivate them. Hence, electrons and lithium-ions can simultaneously pass through the surface film, increasing the potential of the negative electrode. Increased temperatures can cause the surface species to dissolve, thus increasing the electronic conductivity and, in turn, the rate of self-

discharge. Whereas self-discharge is not expected to be important for lithium-ion batteries used in electric vehicles, it can be significant for other applications where the cell remains unused for a considerable period of time in hot ambient conditions. For example, Ehrlich¹⁴ presented self-discharging data for Sanyo C/LiCoO₂ full cells stored at temperatures ranging from 0 to 60°C. The data show relatively little self-discharge for 0 and 25°C ambient temperatures, but significantly more for batteries stored at 60°C. They report 93, 89, and 75% capacity retention after storage at 0, 25, and 40°C, respectively, for 6 months. This result is consistent with the results presented by Johnson and White,²³ which show greater than 97% capacity retention after storage for 1 month at 25°C. In contrast, only 20% of the capacity is retained after 6 months for a 60°C storage temperature. The capacity retention appears to decrease linearly throughout the test period. Hence, if stored at 60°C, the capacity reduces only at a rate of 0.44% per day, which is not significant for HEVs or EVs that are driven frequently. Of course, this rate is dependent on the cell chemistry, but proper electrolyte/electrode combinations should alleviate this relatively small concern.

Thermal runaway.— Thermal runaway occurs in batteries when elevated temperatures trigger heat-generating exothermic reactions, raising the temperature further and potentially triggering more deleterious reactions. Thus, the battery internal temperature increases rapidly if heat is not dissipated effectively. Many researchers have studied the thermal stability of lithium-ion batteries and associated components. The possible exothermic reactions inside the battery have been reviewed by Spotnitz and Franklin.²⁴ The SEI film contains both stable and metastable components, of which the latter decompose exothermically when the temperature rises to values between 90 and 120°C. The SEI normally protects the lithiated carbon from further reaction with the organic electrolyte. Thus, when exposed without a complete SEI, the negative electrode material begins to react exothermically with the solvent at temperatures near 100°C, with the reaction peaking near 200°C (although this reaction may be complicated due to the presence of the salt, typically LiPF₆). Fluorinated binders can also react with the lithiated carbon, but this usually does not occur because the reaction between the negative electrode and the electrolyte occurs first, depleting the available lithium. The positive electrode can also either directly react with the electrolyte or give off oxygen that reacts with the electrolyte. This reaction is highly exothermic, but typically does not occur until high cell temperatures are reached (~180°C, Ref. 25). However, the positive electrode material LiFePO₄ has been shown to exhibit thermal stability superior to that of other electrode materials due to a smaller exothermic heat release.²⁶

Yang et al.²⁷ proposed a general path to thermal runaway in lithium-ion batteries. Once the battery reaches approximately 85°C, the SEI on the graphite negative electrode begins to exothermically decompose. If the temperature then increases to ~110°C, a secondary film begins to form and is successively decomposed. Some of the energy released at this stage may be absorbed by either evaporation of the electrolyte (at ~140°C) or melting of the separator (between 130 and 190°C). These phenomena can cause further problems. For example, typical organic electrolytes used in lithium batteries can readily combust once vaporized if there is available oxygen, which can be evolved from delithiated positive electrodes (e.g., from LiNi_{0.8}Co_{0.15}Al_{0.05}O₂ at 225°C). In addition, a melted separator could cause the battery to short circuit, causing additional heating. The negative electrode graphite reacts at 330°C, releasing some additional heat. Eventually, the aluminum current collector can be melted at 660°C if a catastrophic explosion has not occurred first. Obviously, this scenario can be quite dangerous, especially for large systems, which is one of the primary reasons delaying broad introduction of lithium-ion batteries in the commercial HEV and EV markets.

In addition, the temperature that triggers thermal runaway can vary with the SOC. For example, Al Hallaj et al.²⁸ experimentally studied thermal runaway inside a 1.35 Ah cylindrical Sony battery

with a LiCoO₂ positive electrode. In their calorimeter, they slowly heated the battery in 5°C increments and monitored the temperature of the battery during rest periods to identify the temperature for the onset of thermal runaway. The battery was not connected to any electrical loads, and they conducted tests at several open circuit potentials (OCP): 2.8, 3.0, and 4.06 V. They showed that as the OCP increased, the onset of thermal runaway happened at lower temperatures: 144°C at 2.8 V, 109°C at 3.0 V, and 104°C at 4.06 V. Once the batteries began to self-heat, the OCP plummeted, suggesting an internal short circuit. They point out that the melting temperature of the polyethylene separator (145–150°C) is near the onset of thermal runaway.

Numerical investigations have also provided insights into how a battery design may impact the onset of thermal runaway. Verbrugge²⁹ presented a three-dimensional (3D) thermal model of a solid lithium/polymer electrolyte/vanadium oxide prismatic battery pack. In this model, he assumed that the local current flow can be calculated using the following relationship for the electrolyte ionic conductivity

$$i_x = \sigma_x \left(\frac{V_{\text{stack}}}{L} - NU \right) \quad [1]$$

The electrical conductivity of the cell (σ_x) followed an Arrhenius relationship, which shows that the conductivity of the electrolyte increased with temperature, causing more current to pass through the hotter sections of the battery. This generates more ohmic heat in hotter regions, thus increasing the temperature and allowing even more current to be directed to it. For example, the locations inside the center of the cell were more than 20°C higher than at the cooled edges. This resulted in a doubling of the current passing through the center cells versus the surface cells (~30 vs ~15 mA/cm²). Verbrugge stated that this positive feedback has the potential to lead to thermal runaway and must be monitored.

Chen and Evans³⁰ studied the temperature distribution inside a prismatic lithium-ion battery (LiCoO₂ positive electrode) by numerically solving the 3D transient heat equation. They showed that repeated charging (*C*/0.61^c) and discharging (*C*/0.91) caused heat buildup in the stack such that the temperature rises to a peak of 107°C. Chen and Evans also simulated a thermal runaway event due to a localized hot spot. They assumed that a single cell within the battery stack was discharged across a 1 cm² electrode area in 5 min, creating a volumetric heat generation rate of 2300 W/cm³. (The thickness of the cell is not given.) After a 1 min discharge, the peak battery temperature at the center of the stack reached 180°C.

Recently, Kim et al.³¹ presented both lumped and three-dimensional thermal models that simulated various side reactions inside the battery under abusive conditions (i.e., high external oven temperature and internal short circuit). In their model, the volumetric heat generation arose only from cell component reactions: decomposition of the SEI, negative electrode active material and electrolyte reactions, positive active material and electrolyte reactions, and electrolyte decomposition. Each reaction had assigned activation energy, was proportional to the exponential of temperature, and had a factor limiting the extent of the reaction (e.g., concentration of the active material inside the electrode). No combustion reaction, which would have further sustained the thermal runaway, was modeled. Results from their lumped model showed that the surface area-to-volume (*A/V*) ratio was a critical parameter for determining the onset of thermal runaway in an oven test. For example, a larger *A/V* ratio (i.e., more available heat transfer area per unit volume) caused thermal runaway to be triggered faster at higher oven temperatures (160°C). However, at a lower oven temperature (140°C), thermal runaway was suppressed because the cell could reject heat faster

^c The *C*/1 rate is defined as the discharge current that would discharge the battery in 1 h. Hence, the *C*/0.61 rate corresponds to the *C*/1 rate divided by 0.61.

than it was generated. Furthermore, smaller ratios may delay the onset of thermal runaway because reactants are depleted in the cold center before thermal runaway is triggered.

The type of abuse event can have an impact on the mechanism for thermal runaway. Spotnitz and Franklin²⁴ investigated two battery designs with different positive electrode materials (LiNiCoO₂ and LiMn₂O₄) using a simplified one-dimensional (1D) geometry and subjected to several different events: oven exposure at 175°C, external short circuit, overcharge, nail penetration, and crush. In the oven exposure test, the SEI decomposition reacted first, but had little influence on the progression of thermal runaway. However, the reaction of the negative electrode with the electrolyte provided a considerable amount of heat and limited the amount of heat produced from the same electrode reacting with the binder. Once the reaction between the positive electrode and the electrolyte reached its maximum (near 225°C for LiNiCoO₂ and 265°C for LiMn₂O₄) thermal runaway ensued, denoted by a rapid spike in temperature. In the external short circuit test, ohmic heating in the battery raises the temperature so quickly that thermal runaway from this same reaction between the positive electrode and the electrolyte occurs before the other reactions can progress significantly. In overcharge, lithium cannot intercalate into the negative electrode, which causes lithium plating on the surface. Thermal runaway occurs when this metallic lithium and the negative electrode both react with the electrolyte. In all cases, it appears that the reaction with the fluorinated binder [poly(vinylidene fluoride)] has limited influence on the progression of thermal runaway, which has been shown experimentally.⁵²

In summary, thermal runaway is triggered by portions of the battery reaching critical temperatures that cause the onset of heat-producing exothermic reactions. The onset temperature can vary with chemistry, SOC, and abuse event. Most of the current research on improving lithium-ion battery safety is focused on current-limiting (including shutdown separators) or pressure releasing devices, safer electrolytes and positive electrode materials, or special additives and coatings.³³ However, an appropriate thermal management strategy may provide additional safety by limiting thermal runaway. For example, because of the aforementioned positive feedback between temperature and current, it is necessary that internal portions of the battery with poor thermal contact be cooled adequately. This is also essential for rapidly removing heat from the interior of the cell if an internal short circuit occurs. Otherwise, the internal battery temperature will rise. As suggested by Song and Evans,³⁴ one method of reducing the propensity for thermal runaway is to incorporate internal cooling channels inside large batteries. Finally, as implied by Kim and co-workers and Song and Evans, caution must be exercised in designing the thermal management system such that the design of the battery does not increase the likelihood for thermal runaway if exposed to high temperatures.

Electrical balance.— The single-cell voltage of lithium-ion batteries (~ 3.5 V) is not useful for direct application in EVs and HEVs. Hence, these batteries must be connected in series to provide a useful working voltage. Batteries with mismatched capacities connected in series can cause the pack to produce less energy than actually available. This happens because the weakest cell limits the overall performance of the battery pack. Subsequently charging the same pack will cause the weaker cells to be overcharged. This is extremely dangerous for lithium-ion batteries due to unsafe side reactions (e.g., lithium plating on the negative electrode, or oxygen loss from positive electrodes³⁵) that can lead to thermal runaway. Similarly, when lithium deintercalates from the negative electrode during cell overdischarge (i.e., above negative electrode potentials of 3.566 V vs Li/Li⁺), copper ions may dissolve into the electrolyte. Upon recharging, the reverse reaction can cause copper dendrites to form, which may penetrate the separator and cause it to short circuit.⁸ Even slight overcharge of many lithium-ion batteries is not tolerable, and hence, simply monitoring the total pack voltage on recharge is not acceptable because one cannot observe when the weaker cell is being overcharged. Therefore, the voltage of each cell

(or groups of cells connected in parallel) in a lithium-ion battery pack must be monitored individually to ensure safe operation, and many investigators have proposed a variety of different control schemes to ensure safe operation while maximizing energy delivery and recovery.³⁶⁻³⁹ Kuhn et al.³⁷ showed that for certain batteries, charge equalization can extend usable life. A review of the basic charge equalization schemes was presented by Moore and Schneider.³⁸

Battery capacity can also be a strong function of temperature. Hence, cells at different temperatures inside a battery pack may limit capacity. Dickinson and Swan³⁶ showed that as the temperature of lead-acid battery modules varied, the available capacity varied. As a result, they recommended that all batteries within a pack should be maintained within 35–40°C to maximize life cycle capability and performance. Similar requirements have not been recommended for lithium-ion batteries, but it is suspected that tight control of the operating temperature of each individual cell will also improve performance.

Low temperature performance.— Improvement of low temperature performance is a priority for the development of HEV batteries, as shown by the USDOE's goal of 5 kW of power available at –30°C (see Table I). The poor low temperature performance of NiMH batteries has led to research on efficient battery heating methods (e.g., Ref. 39) and has led commercial HEV manufacturers to employ battery heating strategies.⁴⁰ The exact mechanisms leading to poor performance of lithium-ion batteries at cold temperatures are still not well understood,⁴¹ and a review of these mechanisms is outside the scope of this document. Nonetheless, it is clear that the performance of lithium-ion batteries is reduced at lower temperatures for all cell materials. In addition, the charge performance is substantially less than that for discharge. For example, a typical lithium-ion battery can discharge almost 90% of its rated capacity at a C/5 rate, but cannot accept this same percentage on charging at the same rate and temperature.⁴² Also, due to significant lithium plating at low temperatures, capacity can be irreversibly lost if charged at low temperatures.⁴²

Table IV shows representative low temperature data for both discharging and charging at cold temperatures. It can be seen that the battery capacity drops with temperature, especially below –20°C. Although the ionic conductivity of the SEI and electrolyte and the diffusion of lithium into the graphite can be reduced significantly at low temperatures, Zhang et al.⁴⁴ argue that poor performance of lithium-ion batteries at low temperatures is linked to poor charge transfer at the electrode/electrolyte interface. In fact, this poor charge transfer can lead to significant plating on the negative electrode during charging, which can cause irreversible capacity loss from electrolyte reduction. Fan and Tan⁴² recommended avoiding high charge rates at low temperatures, even at short pulses, to limit capacity fade.

Heat Generation and Thermal Modeling

Because lithium-ion battery performance is strongly linked to temperature, it is important to understand how heat is generated and dissipated inside a battery. Heat generation inside batteries is a complex process that requires understanding of how the electrochemical reaction rates change with time and temperature and how current is distributed within larger batteries. Many investigators have studied thermal heat dissipation characteristics inside both single-cell batteries and multicell battery packs using a variety of assumptions applied to both simple 1D models with uniform heat generation and detailed 3D coupled electrochemical–thermal models. Some investigators have attempted to measure battery heat generation rates using both commercially available and custom-built calorimeters. The use of experimental data is critical to understand the order of magnitude and pattern of the variety of mechanisms that cause batteries to generate heat.

This section discusses the theoretical origins of heat generation inside the battery. In addition, the various measurement techniques

Table IV. Summary of reviewed studies on low temperature performance.

Author	Materials	Test temperature	Discharge rate	Nominal voltage	Capacity metric	Key conclusions
Ehrlich ¹⁴	C/LiMn ₂ O ₄	20°C 0°C -20°C 21°C -20°C	C/5	3.9 3.7 3.5 3.6 3.2	1.4 Ah 1.3 Ah 1.7 Ah 1.5 Ah	
Nagasubramanian ⁴³	Commerical battery	10°C -10°C -20°C -40°C	C/14		320 Wh/L 280 Wh/L 250 Wh/L 10 Wh/L	Impedance spectra suggested slow charge transfer resistance at the electrode/electrolyte interface was responsible for poor low temperature performance
Zhang et al. ⁴¹	C/Li-Ni mixed oxide	20°C -10°C -40°C	C/2		100% 90% 30%	Charge transfer resistance decreased rapidly at low temperature

described in the literature are discussed, leading to important insights about the difficulties in gathering accurate, reliable heat generation data. Finally, the range of methods used to predict rates of heat generation and thermal response inside batteries and the degree of agreement between these predictions and experimental results are reviewed. The purpose of these three subsections is to document and understand the assumptions made by previous authors, trends observed by researchers, and the effectiveness of model simplifications to better understand how heat is generated and dissipated inside lithium batteries. Deficiencies in the literature are documented and discussed, and implications for thermal management are stated.

Origins of battery heat generation.— Heat is produced in batteries from three fundamental sources: activation (interfacial kinetics), concentration (species transport), and ohmic (Joule heating from the movement of charged particles) losses. For small cells, the heat loss from the movement of electrons in the current collectors is usually negligible. However, as the battery increases in size, the length from the current source to the tab and the concentration of current near the tabs may cause significant heat generation (see Fig. 1). In this section, the fundamental expressions for localized electrochemical heat generation are discussed in detail. Based on the currently available literature, recommendations for the correct expression for electrochemical heat generation and its application to larger batteries are provided.

Electrochemical process heat generation.— Bernardi et al.⁴⁵ derived an expression for battery heat using a thermodynamic energy balance on a complete cell. Discrete phases inside the battery interact with each other by means of electrochemical reaction, phase changes, and mixing. By applying the first law of thermodynamics around the cell control volume (not including current collectors) and making numerous simplifications, they determined the following expression for heat generation inside the battery

$$q = -IV - \sum_l I_l T^2 \frac{d \frac{U_{l,avg}}{T}}{dT} + \sum_j \frac{d}{dt} \left[\int_{v_j} \sum_i c_{i,j} R T^2 \frac{\partial}{\partial T} \ln \left(\frac{\gamma_{i,j}}{\gamma_{i,j}^{avg}} \right) dv_j \right] + \sum_{j,j \neq m} \sum_i \left[\left(\Delta H_{i,j \rightarrow m}^0 - R T^2 \frac{d}{dT} \ln \frac{\gamma_{i,m}^{avg}}{\gamma_{i,j}^{avg}} \right) \frac{dn_{i,j}}{dt} \right] \quad [2]$$

Here, the first term is the electrical power produced by the battery. The second term is the sum of producible reversible work and entropic heating from the reaction and is summed over all simultaneously occurring reactions. The third term is heat produced from mixing. Because the reaction rates are not uniform, concentration variations across the battery are developed as the reaction proceeds. When the current is interrupted, the concentration gradients developed inside the battery relax, causing heat to be released or absorbed. Hence, as the concentration profile inside the battery is developed during operation, an apparent relaxation heat will occur and be opposite in sign but equal in magnitude to the heat observed when the current is cut off. This term may be significant if the enthalpy of the mixture as a function of concentration is nonlinear. The final term in the energy balance is heat from material phase changes. The equation proposed by Bernardi et al. is cited frequently in the literature in its simplified form⁴⁶

$$q = I(U - V) - I \left(T \frac{\partial U}{\partial T} \right) \quad [3]$$

This form has been reported previously (e.g., Sherfey and Brenner⁴⁷); some key features are as follows. The first term is the overpotential due to ohmic losses in the cell, charge transfer overpotentials at the interface, and mass transfer limitations. The electrode potential is determined at the average composition. The second term is the entropic heat, and the potential derivative with respect to temperature is often referred to as the entropic heat coefficient. Phase change and mixing effects are neglected in this expression.

In a subsequent study, Rao and Newman⁴⁸ noted that the use of average composition for the electrode open circuit potentials can lead to significant errors when predicting heat generation. They presented two different methodologies for estimating heat generation: a thermodynamic energy balance and a local heat generation method. For the energy balance, they neglected phase change and mixing effects but used the average local concentration in each phase to determine the rate of change of the enthalpy of the species and phases inside the battery. After neglecting the concentration depen-

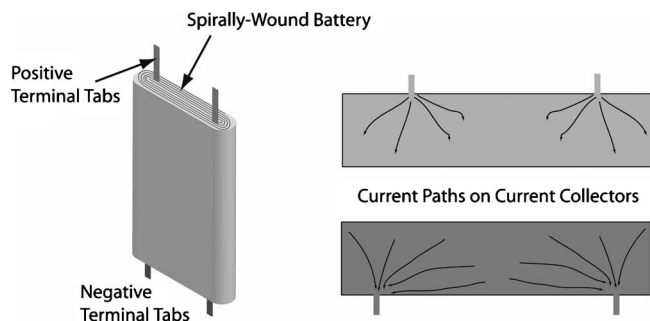


Figure 1. Schematic of spirally wound battery and electron flow paths in the current collectors.

dence of the reference enthalpy and applying Faraday's law (ignoring the electrical double layer), Rao and Newman arrive at the following expression for the battery heat generation

$$q = - \int_v \left(\sum_l a_{i,n,l} U_{H,l} dv \right) - IV \quad [4]$$

The first term in the above expression is the average enthalpy potential (which can include entropic heat effects) integrated where the reactions are actually taking place across the thickness of the battery. They assert that this equation should be used instead of simply using the average composition to determine the open circuit potential.

The local heat generation method derived by Rao and Newman is the summation of all the relevant local thermal effects occurring inside the battery. These include heat generated at the electrochemical interfaces and in the bulk material in different parts of the cell. For this method, Rao and Newman neglect phase changes, concentration gradients in the electrolyte phase, and thermal effects from lithium diffusion. The temperature of the cell is assumed to be uniform. The necessary integration is carried out only normal to the electrode stack (i.e., this is a one-dimensional analysis). The thermal effects include only the Joule heating in the separator and in the electrolyte and matrix in the porous positive electrode (a lithium metal negative electrode was used), as well as the kinetic surface overpotential in both electrodes, resulting in the following

$$-q'' = i(\eta_a + \Delta\phi_s) + \int_{x_1}^{x_2} \left(a_{i,n} \eta_c - i_1 \frac{d\phi_1}{dx} - i_2 \frac{d\phi_2}{dx} \right) dx \quad [5]$$

Rao and Newman show after integrating this expression (over the positive electrode) and applying the appropriate boundary conditions that this expression is equivalent to the energy balance method. (This expression does not include entropic heat effects, but, if inserted, should not change the result due to the appearance of the Peltier coefficient in the interface overpotential, which is equal to the entropic heating term if both electrodes have the same temperature.) They conclude that assuming no concentration gradients in the electrolyte appears to be similar to assuming no mixing effects. However, as discussed below, using the average local concentration for determining the effective open circuit potential is similar to accounting for the apparent mixing in the bulk electrode.⁴⁹ Furthermore, they show that using the open circuit potential at the average composition causes the cell overpotential to be poorly predicted in their specific lithium polymer battery design.

Recently, Thomas and Newman⁴⁹ studied the heat of mixing effect inside a battery containing a porous insertion electrode. They noted that although Rao and Newman stated they neglected mixing effects, they really did account for the heat of mixing inside the bulk electrode through variation in local current density on the effective electrode open circuit potential. However, Thomas and Newman pointed out that this was only one of four possible ways mixing effects occur inside the cell. The remaining modes of mixing heat are from concentration gradients inside the spherical particles, bulk electrolyte, and inside the electrolyte pores of the insertion electrode. Thomas and Newman illustrated the relative magnitudes of these terms using representative calculations on data collected for a Li/LiAl_{0.2}Mn_{1.8}O₄₋₈F_{0.2} battery discharged at the 2C and C/3 rates for 5 min and 3 h, respectively. In both cases, the mixing heat from the cylindrical electrolyte pores was negligible due its small concentration gradients. The mixing heat across the bulk electrodes and electrolyte was more significant, but small compared to the irreversible and reversible heat. This was a different conclusion than that of Rao and Newman because the ionic conductivity used in this study was an order of magnitude higher, which is more representative of commercial organic solvent-based electrolyte batteries.⁴⁹ Although the heat of mixing in the spherical particle at the lower discharge rate was small at C/3, the mixing heat across the spherical particles was significant compared to the sum of irreversible and reversible heats at the higher discharge rate.

To calculate the enthalpy of mixing in each case, Thomas and Newman determined expressions for the difference in enthalpy from the operating state to the relaxed state using a Taylor-series expansion for the molar enthalpy of each species, while neglecting density and temperature changes and concentration dependence on the second derivative of partial molar volume with respect to partial molar enthalpy. For the solid spherical particles, they assumed that the rate of reaction is approximately constant with time (pseudo-steady-state) and the particles had uniform current distribution on the surface. For a constant diffusivity, the enthalpy of mixing for the particle per unit separator area is calculated as follows

$$\Delta H_s = \frac{1}{c_{\text{matrix},\infty} U_{\text{matrix},\infty}} \left. \frac{\partial \bar{H}_{\text{Li}}}{\partial c_{\text{Li}}} \right|_{\infty} \left(\frac{I}{FD_{\text{Li}}} \right)^2 \frac{R_{\text{particle}}^4}{\epsilon_{\text{insertion}} L} \frac{1}{1050} \quad [6]$$

The relaxed state is denoted by ∞ . This expression determines the energy per unit separator area released/absorbed when the concentration gradients inside the particles are allowed to relax. The constant 1050 arises from integration of species concentration. Thomas and Newman pointed out that their tested battery design will have a higher heat of mixing than for commercially made batteries due to their large particle size (20 μm). Thus, it is generally safe to neglect this when estimating volumetric heat generation. However, one can use the above expression to determine if the heat of mixing in the solid particle is important for a particular electrode design.

Heat generation in large batteries.— In addition to electrochemical heat generation, Joule heating is produced from bulk electron movement in the current collectors (see Fig. 1). In small cells, this term may be insignificant. However, increased attention is now being paid to larger cells used in HEVs and EVs, where the electrical distribution in the current collectors may have a large impact on the overall heat generation rate. For example, Kim et al.^{50,51} have investigated the impact of current distribution on several different electrode configurations for a C/LiNiCoMnO₂ polymer electrolyte battery. The two-dimensional (2D) model (variation in the thickness was neglected) consisted of two electrode current collectors coupled via a temperature-independent parameterized electrochemical model, which uses local overpotential to estimate local current production. The current fields in each collector are determined via Ohm's law, and the local volumetric heat generation rate is determined as follows

$$q''' = i''' \left(U - V - T \frac{\partial U}{\partial T} \right) + (\sigma |\nabla \phi|^2)_{\text{cc,pos}} + (\sigma |\nabla \phi|^2)_{\text{cc,neg}} \quad [7]$$

The first term is the electrochemical heat generation (per unit volume), which was discussed in detail above. The last two terms are the resistive heating due to current movement in the positive and negative metal current collectors, respectively. If the tab locations are designed appropriately, the distribution of local current generation from the electrochemical reaction may be minimally impacted. However, even though current production and overpotential may be similar, increased current is passing through the battery locally, which increases resistive heating in the current collectors. For example, in Kim et al.'s first study, a ~ 87 mm wide and ~ 150 mm tall cell with 35 mm wide current collector tabs placed on the top end of the current collectors caused less than 0.5% maldistribution in current when discharged at the 1C rate for 30 min. However, both the simulation and experiments show a more than 17°C temperature variation, with the hottest portions of the battery near the current collection tabs. The recent work at the National Renewable Energy Lab (NREL) that includes solving electrochemical transport locally has also shown similar results.^{52,53}

In summary, the heat generation estimated by Bernardi et al. (Eq. 3) is the most commonly used equation to estimate battery heat generation. This equation may be readily applied to estimate the amount of electrochemical heat generation in small lithium-ion batteries if there is no heat from mixing or phase change, no spatial variation in temperature or SOC, only one electrochemical reaction

Table V. Summary of battery heat generation test methods.

Investigators	Heat rejection from battery	Special data processing
<i>ARC — measurement of battery and calorimeter surface temperature</i>		
Al Hallaj et al. ⁵⁴	Conduction through Styrofoam	Experimentally determined calorimeter constant
Al Hallaj et al. ⁵⁵	Natural convection and radiation through air	Experimentally determined calorimeter constant
Hong et al. ⁵⁶	Conduction through Styrofoam	Experimentally determined calorimeter constant
<i>IHC — measurement of thermopile temperature difference</i>		
Bang et al. ⁵⁷	Conduction through isothermal heat sink (bottom only)	Difference between test cell and dummy cell is the heat rate
Kim et al. ⁵⁸	Conduction through aluminum heat sink	300 s time lag correction
Kobayashi et al. ⁵⁹	Conduction through isothermal heat sink (bottom only)	Neglected 600 s instrument time lag
Kobayashi et al. ⁶⁰	Conduction through isothermal heat sink (bottom only)	None given
Lu and Prakash ⁶¹	Not given (isothermal bath)	Time lag correction (no specific time value given)
Lu et al. ⁶²	Not given (isothermal bath)	Self-discharge correction
Lu et al. ⁶³	Not given	None given
Lu et al. ⁶⁴	Not given	None given
Onda et al. ⁶⁵	Convection through isothermal water bath	None given
Saito et al. ⁶⁶	Conduction through temperature-controlled heat sink	341 s time lag correction
Saito et al. ⁶⁷	Not given	420 to 460 s time lag correction
Song and Evans ⁶⁸	Not given (isothermal bath)	None given
Thomas and Newman ⁴⁹	Conduction through copper shot	Numerical convolution of data, equipment offset correction, 300 s time lag correction
Yang and Prakash ⁶⁹	Not given	Subtracted constant value instrument offset
<i>RC — measurement of applied heater power, cell temperature, and lead-wire temperature</i>		
Vaidyanathan et al. ⁷⁰	Radiation through vacuum through copper chamber (−168°C by liquid N ₂)	External heat applied and wire lead heat loss correction

occurring at each electrode, and negligible Joule heating in the current collectors. In lithium-ion batteries without side reactions, there is only one reaction occurring at each electrode, and no phase change effects exist. Neglecting the heat of mixing terms is acceptable for low discharge rates, and will be for high discharge rates when the particle size is sufficiently small, which is representative of commercial battery designs. In large battery simulations, the electrochemical reactions may be sufficiently nonuniform for poorly placed current collection tabs, which result in both SOC and temperature nonuniformities. However, resistance heating in the current collectors of large batteries may be significant relative to the electrochemical heat generation rate for even well designed batteries that have uniform current production and working potential across the cell throughout the battery. In these cases, discretization of the battery into smaller cells and accounting for current collector Joule heating is imperative. Thus, it is recommended that Eq. 7 be used to simulate heat generation in batteries.

Battery heat generation experiments.— This section describes the various techniques used to measure the heat generation rate in lithium-based batteries. The purposes of this section are to assess the ranges of temperature and discharge/charge rates addressed by previous researchers, to understand the magnitudes of overpotential and entropic heat generation rates, and to evaluate the methods used to measure the heat rates.

Total volumetric heat rate.— Table V shows a summary of different techniques used to measure heat generation rate in lithium-ion battery half and full cells during charge and discharge. This table includes the experimental technique along with a short description of how heat is removed and measured from the battery during the test.

The primary experimental methods are accelerated-rate calorimetry (ARC) and isothermal heat conduction calorimetry (IHC). The ARC method consists of measuring the heat rejected from the battery surface through air or Styrofoam to a constant temperature sink. In this method, the temperature of the battery is allowed to rise during operation, and the heat generation rate is estimated using an energy balance on the battery as follows⁵⁶

$$q = MC_p \frac{dT}{dt} + hA(T_{\text{surf}} - T_{\text{well}}) \quad [8]$$

The first term is the amount of heat stored inside the battery, while the latter is the heat transferred from the surface of the battery to the constant temperature well. The calorimeter constant (hA) and the effective heat capacity of the cell are determined experimentally.^{55,56} For IHC, the battery remains at one temperature throughout operation using an isothermal well in close contact with the surface of the battery (e.g., liquid or a metal heat sink). High accuracy thermopiles either embedded inside the heat sink or placed near the surface of the battery are used to measure the heat rate. As in all calorimetric methods, special data processing or experimental procedures are usually required due to the long instrument time constants (i.e., time elapsed from heat generation to measurement). For example, Thomas and Newman⁴⁹ numerically integrated a convolution integral using an approximate Dirac delta function estimated from a previous experiment and also added the 300 s time lag to the deconvoluted heat generation rate to facilitate comparison with their model results. In contrast, Kobayashi et al.⁶⁰ simply discharged at slow rates ($< C/10$) and neglected the 600 s time constant. Self-discharge can be important for these long discharge times and complicate the

Table VI. Gap analysis of battery heat generation test methods.

Collection Method	Charge or Discharge	< C/10	C/10 ≤ I ≤ C/1	> C/1
ARC	Charge	●	●	
	Discharge	●	●	■
IHC	Charge	●	●	▲
	Discharge	●	●	▲
RAD	Charge	●	●	
	Discharge	●	●	

Legend:

Square = prismatic cell; Circle = cylindrical cell; Triangle = coin cell

Bottom half = positive electrode; Top half = negative electrode

Materials:

carbon insertion compound (black), lithium metal (white), lithiated metal oxide (gray)

analysis. For example, Lu et al.⁶² corrected their data from the self-discharge observed at high positive electrode potentials.

Radiation calorimetry (RC) is achieved by suspending the battery in an evacuated constant-temperature container. The energy balance on the battery is as follows

$$q = MC_p \frac{dT}{dt} + \varepsilon \sigma_{\text{SB}} A (T_{\text{surf}}^4 - T_{\text{env}}^4) + \frac{k_{\text{wire}} A_{\text{cwire}}}{L_{\text{wire}}} (T_{\text{surf}} - T_{\text{wire}}) - q_{\text{heater}} \quad [9]$$

The first three terms on the right side are the heat accumulated in the battery, radiation heat lost from the battery to the constant temperature container, and conductive loss through the lead wires, respectively. The last term is the heat applied to maintain a constant battery temperature while at rest.

To facilitate discussion of these methods, Table VI shows a gap analysis that includes the geometry, chemistry, and discharge/charge rates tested. As shown, the majority of previous studies on insertion electrodes for lithium-ion batteries have been conducted on small coin cells for low to moderate discharge rates (i.e., C/10 to C/1). There are few studies conducted for discharge rates > C/1. This emphasizes the difficulty in measuring transient high rate heat generation. The fast heating of the cells can rapidly increase the internal temperature of the battery. This makes the heat storage term the most significant value in the energy balance, thus requiring the battery heat capacity to be precisely measured. In addition, for large batteries, significant thermal gradients inside the cell may develop, thus requiring more careful experimental techniques. Moreover, the multiple studies on low rate discharge of coin cells are attempts to measure the entropic heat coefficient. This is achieved relatively easily because the low heating rates minimize temperature rise. In addition, the coin cells are thermally thin, thus substantially reducing internal temperature gradients that can influence the results.

Tables VII-IX show a summary of the battery tests and the measured volumetric heat generation rates for charge and discharge, respectively, as a function of rate for the reviewed studies. The most important term for thermal simulation of batteries is the volumetric heat generation rate. However, because no investigations actually report the heat rate on a volume basis, cross-study comparison requires significant manipulation of the reported data. This includes estimating the heat rate from the total cell volume,^{54-56,59-68,70} from the thickness of the unit cell⁴⁹ or the entire battery,⁶⁹ or from standard densities of full cells.^{57,58} Unfortunately, these assumptions can greatly influence the estimated volumetric heat generation rate. For example, Yang and Prakash⁶⁹ reported the heat generation rate per unit separator area ($\mu\text{W}/\text{cm}^2$) for a 2032 coin cell (i.e., 20 mm

outside diameter (OD) and 3.2 mm height). If one uses the total cell thickness (3.2 mm), the heat generation rate for the C/1 discharge ranges from 0 to 0.62 W/L. In reality, the unit cell may be a factor of 10 (or more) smaller, thus changing the results to 0–6.2 W/L. Furthermore, the values reported contain wide variability from study to study, even for the same chemistry. For example, Onda et al.⁶⁵ and Al Hallaj et al.⁵⁵ gathered data on the same commercial cylindrical cell (Sony 18650, C/LiCoO₂) using two different techniques: IHC and ARC, respectively. Onda and co-workers reported heat generation rates ranging from 13.3 to 84.5 W/L for a 0.92C discharge rate, whereas Al Hallaj and co-workers reported 0.0 to 15.5 W/L for a C/1 discharge rate.

Cross-comparison of chemistry, rates, and measurement techniques is a particularly difficult task for the following reasons: large discrepancies appear from study to study (even using the same batteries), and no investigation reports volumetric heat generation rate directly. Nevertheless, a few general statements about the previously reported results can be made. First, the heat rates are a strong function of the discharge rate. For example, in the study of Onda et al.⁶⁵ the heat rate ranges from –0.45 to 11.0 W/L and from 13.3 to 84.5 W/L for the C/10 and 0.92C discharge rates, respectively. The negative value reflects the impact of entropic heating, which is discussed below. Second, there is an extremely wide range of reported peak values at the same discharge rate. For example, peak rates ranging from 0.31 to 84.5 W/L are reported for the C/1 discharge. Without knowledge of the geometric details or the uncertainty in the reported values, it cannot be known if these differences are real or artifacts of testing method and/or data reduction choices. Third, the heat rate increases as the battery is discharged further for moderately high discharge rates, but the profile differs between the studies. For example, the studies by Al Hallaj and co-workers⁵⁴⁻⁵⁶ show that the heat rates increases monotonically as the battery is discharged. However, the studies of Bang et al.,⁵⁷ Kim et al.,⁵⁸ and Onda et al.⁶⁵ show that the heat rate follows an S-shaped curve as the battery is discharged. The profiles appear to be dependent on the relative magnitude of the entropic and overpotential heats, which is discussed in more detail below. Finally, the majority of studies has been conducted at one temperature (near nominal ambient: 20–25°C), and few studies have investigated the impact of temperature on heat generation. For those that have investigated temperature influences, the range of temperatures is typically small. The studies of Saito et al.⁶⁶ and Kobayashi et al.⁵⁹ have the largest temperature ranges (20–60°C and 25–60°C, respectively), but they only tested batteries discharged at low current (C/10). Thomas and Newman⁴⁹ and Hong et al.⁵⁶ tested higher rates, but with a more narrow temperature spread (15–30°C and 35–55°C, respectively). In both of these studies, no appreciable difference in heat generation was observed for the temperatures tested. However, it is expected that as the test temperature range broadens, the heat generation rate will be seen as a strong function of temperature as the discharge rate increases. As discussed below, the cell overpotential generally decreases with cell temperature due to improved mass transport and kinetics, which should reduce its heat generation rate. However, at low rates, the reversible heat can be relatively large, and it is not a strong function of temperature. Thus, an investigation that measures heat generation rate over a wider range of test temperatures at higher rates is warranted.

Reversible heat rate.— As stated above, there have been many investigations that measure the entropic heat generation. In general, a variety of conclusions have been drawn about the importance of including entropic heat in the energy balance in thermal models. In this section, the different techniques used to estimate the entropic heat coefficient are reviewed, and the magnitudes for several relevant lithium-ion battery chemistries are analyzed.

Several methods are used to estimate the entropic heat coefficient (i.e., dU/dT). The most common method is to measure the OCP variation with temperature at a fixed SOC.^{54-57,61,62,65,69,71,72} This is the most straightforward and easiest method to implement, but it does have a few minor drawbacks that have led other investigators

Table VII. Summary of battery tests: battery geometry, material, tested currents, and temperatures.

Investigators	Battery description		Currents	Temperatures
	Geometry	Material		
Al Hallaj et al. ⁵⁴	Cylindrical cell: 18 mm OD, 65 mm height Coin cell: 20 mm OD, 1.6 mm height	Half coin cell: C/Li Full cylindrical cells: C/LiCo _{0.2} Ni _{0.8} O ₂ (graphite) C/LiCoO ₂ (A—graphite, B—hard carbon, C—graphitized carbon fiber)	C/30 to C/1	35°C
Al Hallaj et al. ⁵⁵	Cylindrical cell: 18 mm OD, 65 mm height Prismatic cell: (D) 46 mm × 29 mm × 5 mm (E) 46 mm × 33 mm × 12 mm	Full cells: C/LiCoO ₂ (A—graphite, B—hard carbon, C/D/E—graphitized carbon fiber)	C/12 to 2C	35°C
Hong et al. ⁵⁶	Cylindrical cell: 18 mm OD, 65 mm height	Full cell: C/LiCoO ₂ (hard carbon, Sony)	C/1 to C/3	35°C to 55°C
Bang et al. ⁵⁷	Coin cell: 20 mm OD, 3.2 mm height	Half cells: Li/LiMn ₂ O ₄ and Li/LiAl _{0.17} Mn _{1.83} O _{3.97} S _{0.03}	C/10 to C/1	25°C
Kim et al. ⁵⁸	Coin cell: 20 mm OD, 1.6 mm height	Half cell: Li/LiMn ₂ O ₄	C/10 to C/1	25°C
Kobayashi et al. ⁵⁹	Prismatic cell: 26 mm × 9 mm × 48 mm Cylindrical cell: 18 mm OD, 65 mm height	Full prismatic cell: C/LiMn ₂ O ₄ Full cylindrical cell: C/LiCoO ₂	C/50, C/10	25°C to 60°C
Kobayashi et al. ⁶⁰	Cylindrical cell: 18 mm OD, 65 mm height Coin cell: 20 mm OD, 3.2 mm height	Half coin cells: C/Li and Li/LiCoO ₂ Full cylindrical and coin cells: C/LiCoO ₂	C/50, C/30, C/25	not given
Lu and Prakash ⁶¹	Coin cell: 20 mm OD, 3.2 mm height	Half cell: C/Li (MCMB)	C/10 to C/1	25°C
Lu et al. ⁶²	Coin cell: 20 mm OD, 3.2 mm height	Half cell: Li/Li _{1+x} [Ni _{1/3} Co _{1/3} Mn _{1/3}] _{1-x} O ₂	C/5	25°C
Lu et al. ⁶³	Coin cell: 20 mm OD, 3.2 mm height	Half cells: Li/LiNi _{0.8} Co _{0.2} O ₂ and C/Li Full cell: C/LiNi _{0.8} Co _{0.2} O ₂ (MCMB)	C/10 to C/1	25°C
Lu et al. ⁶⁴	Coin cell: 20 mm OD, 3.2 mm height	Half cells: Li/LiMn ₂ O ₄ , Li/Li _{1.06} Mn _{1.89} Al _{0.05} O ₄ , and Li _{1.156} Mn _{1.844} O ₄ cells	C/10	10°C
Onda et al. ⁶⁵	Cylindrical cell: 18 mm OD, 65 mm height	Full cells: C/LiCoO ₂ (A—hard carbon, B—graphite)	0.1C to 0.92C	30°C
Saito et al. ⁶⁶	Cylindrical cell: 14 mm OD, 50 mm height	Full cells: C/LiCoO ₂ (hard carbon)	C/10	20°C to 60°C
Saito et al. ⁶⁷	Cylindrical cell: 18 mm OD, 65 mm height	Full cells: C/LiCoO ₂ (A/B/C—graphite, D—hard carbon)	0.037C, 0.04C	40°C
Song and Evans ⁶⁸	0.21 mm unit cell and 2 cm ² area	Half cell: Li/LiMn ₂ O ₄	C/2 to 5C/3	90°C
Thomas and Newman ⁴⁹	Coin cell: 23 mm OD, 2.5 height	Half cell: Li/LiAl _{0.2} Mn _{1.8} O _{4-δ} F _{0.2}	C/8 to 2C	15°C to 30°C
Yang and Prakash ⁶⁹	Coin cell: 20 mm OD, 3.2 mm height	Half cells: Li/LiNi _{0.8} Co _{0.15} Al _{0.05} O ₂ and C/Li Full cells: C/LiNi _{0.8} Co _{0.15} Al _{0.05} O ₂ (natural graphite Mag-10)	C/20 to C/1	25°C
Vaidyanathan et al. ⁷⁰	Cylindrical cell: 18 mm OD, 65 mm height	Full cells: C/LiNiO ₂ and C/LiCoO ₂ (75%) and LiNiO ₂ (25%)	C/61.7 to C/1	0°C, 15°C

to explore other methods. First, long times are required to ensure that the OCP is steady. For example, Onda and co-workers^{65,71} waited 3 h at each SOC tested (e.g., six test points in Ref. 65) at four different test temperatures (10, 20, 30, and 40°C). This results in at least 72 h of required testing for one battery. Yang and Prakash,⁶⁹ Lu et al.,⁶³ and Lu and Prakash⁶¹ considered the voltage stabilized within ± 0.1 mV/min, but the relaxation time was still

approximately 2 h.⁶⁹ Furthermore, self-discharge can be important at these long wait times, especially at a high SOC. Lu et al.,⁶⁴ Hong et al.,⁵⁶ and Onda et al.⁷¹ all had difficulties maintaining stable voltages for a high SOC. Subsequently, Thomas et al.⁷³ developed another technique to minimize the effect of self-discharge. In their study, they discharged a fully charged cell to a specific SOC, followed by a charge/discharge cycle at a very slow rate (C/100) with

Table VIII. Summary of battery tests: charging heat generation.

Investigators	Cell type	Heat generation rates (W/L)				
		$< C/10$	$C/10 \leq I \leq C/5$	$C/5 < I < C/2$	$C/2 \leq I \leq C/1$	$> C/1$
Al Hallaj et al. ⁵⁴	Cylindrical	−0.51 to 0.26				
Hong et al. ⁵⁶	Cylindrical			−2.27 to 1.63		
Bang et al. ⁵⁷	Coin 1		−0.17 to 0.63	0.03 to 2.65	0.11 to 7.51	
	Coin 2		−0.05 to 1.11			
			−0.08 to 0.82	0.00 to 4.41	0.00 to 14.9	
			0.00 to 1.32			
Kim et al. ⁵⁸	Coin		−0.08 to 0.49	0.47 to 0.97	−0.08 to 3.21	
			−0.36 to 0.58			
Kobayashi et al. ⁵⁹	Cylindrical		−1.31 to 0.97			
	Prismatic	−0.15 to 0.15	−0.63 to 0.76			
Kobayashi et al. ⁶⁰	Coin 1	0.00 to 0.02				
	Coin 2	−0.03 to 0.01				
	Coin 3	−0.03 to 0.00				
Lu and Prakash ⁶¹	Coin		−0.01 to 0.04	0.00 to 0.08	0.00 to 0.35	
Lu et al. ⁶²	Coin		0.01 to 0.02			
Lu et al. ⁶³	Coin 1		0.00 to 0.02	0.02 to 0.10	0.24 to 0.73	
	Coin 2		−0.01 to 0.03	−0.02 to 0.07	0.00 to 0.32	
	Coin 3		−0.02 to 0.02	−0.01 to 0.07	0.00 to 0.40	
Lu et al. ⁶⁴	Coin 1		0.00 to 0.02			
	Coin 2		0.00 to 0.01			
	Coin 3		0.00 to 0.01			
Saito et al. ⁶⁷	Cylindrical 1	−1.01 to 0				
	Cylindrical 2	−0.76 to 0.45				
	Cylindrical 3	−1.21 to 0.45				
	Cylindrical 4	−0.05 to 0.11				
Thomas and Newman ⁴⁹	Coin		−1.33 to 1.82	−1.27 to 5.69		9.01 to 18.8
Yang and Prakash ⁶⁹	Coin 1	0.00 to 0.01	0.00 to 0.02	0.00 to 0.04	0.00 to 0.60	
	Coin 2	−0.02 to 0.02	−0.05 to 0.05	−0.07 to 0.12	−0.09 to 1.07	
	Coin 3	−0.02 to 0.00	−0.04 to 0.02	−0.06 to 0.06	0.00 to 0.41	
Vaidyanathan et al. ⁷⁰	Cylindrical 1		−0.60 to 1.95			
	Cylindrical 2	−0.48 to 0.00	1.00 (average)			

rest periods in between (4 min after the charge and 20 min after the discharge). During the rest period, the temperature of the cell was varied between 21 and 29°C at a ramp rate of approximately 0.3°C/min using a water bath. The slope of the voltage versus temperature curve (and, hence, the entropic heat coefficient) was estimated during the rest period. The process is repeated for multiple SOC's. Even for this short duration test, the problem of self-discharge for this cell (doped and undoped LiMn_2O_4 positive electrodes) was evident for OCP's greater than 4.2 V. To compensate for self-discharge, they subtracted a voltage profile for a battery held at constant temperature from the variable temperature data, which yielded a linear relationship between voltage and temperature.

The other methods are calorimeter-based. First, several authors assumed that irreversible heat remained constant upon charge and discharge. Hence, they subtracted the charge calorimeter data from the discharge data, which cancels the overpotential heat, and allows for the entropic heat to be determined as follows

$$q_{\text{ent}} = \frac{q_{\text{dis}} - q_{\text{cha}}}{2} \quad [10]$$

Thomas et al.⁷³ showed that this method provided similar results to their SOC cycling method described above. Onda et al.⁶⁵ also showed that this method produced results similar to those of the direct measurement of OCP versus temperature. However, Hong et al.⁵⁶ observed that this method produced entropic heat coefficients that were a function of rate, which may be attributable to inaccuracies in their measurement technique. Another calorimetric method is to subtract an estimated irreversible heat from the total heat. The overpotential heat is typically (and most accurately) estimated by direct calculation of the overpotential using OCP and operating voltage data.⁶¹⁻⁶⁴

Table X summarizes previous investigations that estimate entropic heat for electrodes used in lithium-ion batteries. Each material investigated is also listed, and half cells mean that lithium metal is the counter electrode. The data show that the entropic heat coefficients of each material tested lie within ± 1 mV/K and that the values can switch from negative (exothermic on discharge) to positive (endothermic on discharge) as the electrode is cycled from 0 to 100% SOC. For the positive electrode materials (i.e., the metal oxides), the switch from negative to positive can coincide with crystalline phase changes or different lithium insertion/deinsertion staging. For example, Al Hallaj et al.⁵⁴ used the phase diagram of Reimers and Dahn⁷⁴ for LiCoO_2 to show that the increase–decrease–increase in a surface temperature trace of a Panasonic 18650 cell was caused by the crystalline phase change from hexagonal to monoclinic to hexagonal. In addition, the order at which the sublattice in LiMn_2O_4 is filled with lithium ions is dependent on the SOC, which affects the observed heat: endothermic when nearly empty and exothermic when the nearest sublattice is full for discharging.⁷³ Doping agents can affect the nature of the order/disorder in various materials.^{62,64,73} In the carbon negative electrode, the type of carbon can affect the entropic heat coefficient. For example, the full cells with coke-based carbon negative electrodes tested by Hong et al.⁵⁶ have primarily negative coefficients whereas other investigations with the same positive electrode material (LiCoO_2) but different types of negative electrodes have coefficients that can switch from positive to negative. Lu and Prakash⁶¹ and Thomas and Newman⁷² have both suggested that the entropic coefficient for the MCMB's negative electrode was mostly negative but became positive at the end of discharge due to the different lithium staging.

Table IX. Summary of battery tests: discharging heat generation.

Investigators	Cell type	Heat generation rates (W/L)				
		$< C/10$	$C/10 \leq I \leq C/5$	$C/5 < I < C/2$	$C/2 \leq I \leq C/1$	$> C/1$
Al Hallaj et al. ⁵⁴	Cylindrical	-0.24 to 0.59				
Al Hallaj et al. ⁵⁵	Cylindrical 1		0.00 to 1.89	0.00 to 5.29	0.00 to 7.68 0.00 to 15.5	
	Cylindrical 2		0.00 to 6.55	0.00 to 10.3	0.00 to 15.1 0.00 to 27.7	
	Cylindrical 3		0.00 to 2.27	0.00 to 4.53	0.00 to 6.58 0.00 to 13.2	
	Cylindrical 4		0.00 to 2.50	0.00 to 4.38	0.00 to 14.1	0.00 to 30.3
	Cylindrical 5		0.00 to 2.74	0.00 to 9.08	0.00 to 19.6	0.00 to 26.8
Hong et al. ⁵⁶	Cylindrical			0 to 12.1	0 to 16.1 0 to 33.3	
Bang et al. ⁵⁷	Coin 1		-0.17 to 1.15 -0.20 to 1.97	-0.05 to 4.75	-0.05 to 10.2	
	Coin 2		-0.12 to 0.57 0.00 to 0.77	0.00 to 1.81	0.00 to 8.11	
Kim et al. ⁵⁸	Coin		-0.14 to 0.41 -0.32 to 0.95	-0.32 to 1.77	0.00 to 5.71	
Kobayashi et al. ⁵⁹	Cylindrical					
	Prismatic	-0.04 to 0.24				
Kobayashi et al. ⁶⁰	Coin 1	-0.01 to 0.05				
	Coin 2	0.01 to 0.06				
	Coin 3	0.00 to 0.05				
	Cylindrical	-0.56 to 0.32				
Lu and Prakash ⁶¹	Coin		-0.01 to 0.03	-0.01 to 0.07	0.00 to 0.31	
Lu et al. ⁶²	Coin		-0.01 to 0.00			
Lu et al. ⁶³	Coin 1		0.00 to 0.08	0.91 to 0.20	0.13 to 0.80	
	Coin 2		-0.01 to 0.03	0.00 to 0.08	0.00 to 0.37	
	Coin 3		-0.01 to 0.04	-0.01 to 0.13	0.00 to 0.59	
Lu et al. ⁶⁴	Coin 1		0.00 to 0.02			
	Coin 2		0.00 to 0.01			
	Coin 3		0.00 to 0.02			
Onda et al. ⁶⁵	Cylindrical		-0.45 to 11.0	-0.45 to 27.5 4.12 to 44.0	13.3 to 84.5	
Saito et al. ⁶⁶	Cylindrical		0.79 to 3.90			
Saito et al. ⁶⁷	Cylindrical 1	0.08 to 1.80				
	Cylindrical 2	-0.30 to 2.04				
	Cylindrical 3	-0.23 to 2.47				
	Cylindrical 4	0.11 to 1.95				
Song and Evans ⁶⁸	Coin				1.42 to 9.05 2.38 to 16.4	5.00 to 31.4
Thomas and Newman ⁴⁹	Coin		-0.11 to 2.38	0.00 to 7.85		13.1 to 16.6
Yang and Prakash ⁶⁹	Coin 1	0.00 to 0.02	0.00 to 0.06	0.00 to 0.07	0.00 to 0.40	
	Coin 2	-0.01 to 0.04	-0.02 to 0.07	-0.03 to 0.15	0.00 to 0.61	
	Coin 3	-0.01 to 0.04	-0.01 to 0.09	-0.03 to 0.20	0.00 to 0.62	
Vaidyanathan et al. ⁷⁰	Cylindrical 1		0.00 to 2.67		0.00 to 11.2 0.00 to 22.0	
	Cylindrical 2			0.00 to 10.1	0.00 to 17.0 0.00 to 40.1	

Table XI presents a comparison between heat generation from overpotential at the $C/1$ rate and the entropic heat at a nominal ambient temperature (300 K). This is accomplished by comparing the overpotential directly with the effective potential difference from entropic heat effects (i.e., $T \times dU/dT$). Negative values reported for the entropic heat denote exothermic on discharge and endothermic on charge, but positive values for the resistance indicate exothermic heat generation. Hence, the negative of the entropic heat is presented in Table XI. The results show that most of the heat at the $C/1$ rate is due to overpotential, but the entropic heat is significant, although it is difficult to assess the impact of the entropic heat using only the data in the table. This is because the overpotential increases steadily throughout most of the charge/discharge followed by a dramatic increase at the end, whereas the entropic heat may be a maximum (or minimum) at any SOC. On the other hand, battery surface temperature traces can be used to qualitatively assess the impact of

entropic heating, and the data show evidence that the entropic heat is significant, even at high discharge rates. For example, the data presented by Al Hallaj et al.⁵⁴ showed that the Panasonic cell temperature did not increase steadily but showed oscillations during the beginning of discharge even for rates as high as a $C/1$. This clearly coincided with the cooling effect observed from the LiCoO_2 crystalline phase change. Similarly, the 0.92C temperature trace for the battery tested by Onda et al.⁶⁵ showed a distinct oscillatory temperature profile during the beginning of discharge. In addition, the temperature profile presented by Thomas and Newman⁴⁹ appeared to be a strong function of the entropic heat for the $C/3$ rate, and the data on the LiMn_2O_4 spinel presented by Kim et al.⁵⁸ also showed a strong influence of the entropic heat for the $C/1$ rate. In contrast, the impact of the entropic heat can also be much less. For instance, the heat rate profiles shown by Lu and Prakash⁶¹ appear to be impacted by the entropic heat for the $C/10$ and $C/4$ rates, but there is almost

Table X. Summary of entropic heat test methods.

Study	Material	Capacity	Entropic Heat	
			Methodology	dU/dT (mV/K)
Al Hallaj et al. ⁵⁴	Half cell: C/Li	3.2 mA	Measure dU/dT directly	−0.09 to 0.48
Al Hallaj et al. ⁵⁵	Full cell: C/LiCoO ₂ (graphite)	1.50 Ah	Measure dU/dT directly	−0.75 to 0.23
	Full cell: C/LiCoO ₂ (graphitized carbon fiber)	1.35 Ah		−0.98 to −0.16
	Full cell: C/LiCoO ₂ (graphitized carbon fiber)	0.60 Ah		−0.98 to −0.16
Hong et al. ⁵⁶	Full cell: C/LiCoO ₂ (hard carbon)	1.35 Ah	(a) Measure dU/dT directly (b) Subtract charge from discharge heat	(a) −0.75 to −0.43 (b) −0.84 to −0.42
			Measure dU/dT directly	−0.44 to 0.18
Bang et al. ⁵⁷	Half cell: Li/LiMn ₂ O ₄	Not given		−0.51 to 0.05
	Half cell: Li/LiAl _{0.17} Mn _{1.83} O _{3.97} S _{0.03}			
Lu and Prakash ⁶¹	Half cell: C/Li (MCMB)	Not given	(a) Measure dU/dT directly (b) Subtract overpotential heat	(a) −0.10 to 0.28 (b) −0.16 to 0.30
Lu et al. ⁶²	Half cell: Li/Li _{1+x} [Ni _{1/3} Co _{1/3} Mn _{1/3}] _{1-x} O ₂	1.89 mAh	(a) Measure dU/dT directly (b) Subtract overpotential heat	(a) −0.13 to 0.06 (b) −0.15 to −0.08
Lu et al. ⁶³	Half cell: Li/LiNi _{0.8} Co _{0.2} O ₂	Not given	Subtract overpotential heat	−0.08 to 0.02
	Half cell: C/Li (MCMB)			−0.10 to 0.28
	Full cell: C/LiNi _{0.8} Co _{0.2} O ₂ (MCMB)			−0.30 to 0.20
Lu et al. ⁶⁴	Half cell: Li/LiMn ₂ O ₄	Not given	Subtract overpotential heat	−0.22 to 0.11
	Half cell: Li/Li _{1.06} Mn _{1.89} Al _{0.05} O ₄			−0.13 to 0.13
	Half cell: Li/Li _{1.156} Mn _{1.844} O ₄ cells			−0.10 to 0.08
Onda et al. ⁶⁵	Full cell: C/LiCoO ₂ (hard carbon)	1.35 Ah	(a) Measure dU/dT directly (b) Subtract charge from discharge heat	(a) −0.52 to −0.19 (b) −0.66 to −0.08
	Full cell: C/LiCoO ₂ (graphite)	1.8 Ah		(a) −0.81 to 0.21
	Full cell: C/LiCoO ₂			
Onda et al. ⁷¹	Full cell: C/LiCoO ₂	1.80 Ah	Measure dU/dT directly	−0.66 to 0.02
Thomas and Newman ⁴⁹	Half cell: Li/LiAl _{0.2} Mn _{1.8} O _{4-δ} F _{0.2}	Not given	(a) Measure dU/dT directly (b) Subtract charge from discharge heat	(a) −0.4 to 0.10 (b) −0.22 to 0.10
	Half cell: Li/LiMn ₂ O ₄			(a) −0.35 to 0.25
Yang and Prakash ⁶⁹	Half cell: Li/LiNi _{0.8} Co _{0.15} Al _{0.05} O ₂	1.372 mAh/cm ²	Measure dU/dT	−0.08 to 0.02
	Half cell: C/Li (natural graphite, MAG-10)			−0.26 to 0.55
	Full cell: C/LiNi _{0.8} Co _{0.15} Al _{0.05} O ₂ (natural graphite Mag-10)			−0.38 to 0.18

no effect on the $C/1$ rate data, except that the heat rates for charge and discharge appear to be slightly offset. Similarly, Yang and Prakash⁶⁹ observed that the entropic heat for their full cell contributed to only 5% of the total heat generation.

Analysis of experimental methods.— This section describes some conclusions and observations drawn from previous investigations on experimental methods used to measure heat generation. First, heat is measured primarily at the outer surface of the battery. For the ARC method, this is complicated by the need to estimate the amount of heat stored. Moreover, substantial instrument time lags exist for all of the reported measurement techniques. Both of these drawbacks may have contributed to the fact that very few studies measure heat

generation at high rates (i.e., above $C/1$). Furthermore, increased rates will cause concentration gradients to develop, which can change the local heat generation rate at high discharge rates. This can be observed in the heat rate measurements of Al Hallaj et al.,⁵⁵ Kim et al.,⁵⁸ and Hong et al.,⁵⁶ which show significant heat rejection after the current is stopped. Similarly, Thomas and Newman⁴⁹ observed an overprediction by their model of the experimental data for short-duration pulse discharge at 2C, which they attributed to neglecting heat of mixing within the solid particles, but this was attributed to large particle sizes that probably will not be utilized in commercial EV and HEV battery applications. Furthermore, their analysis showed that the heat of mixing is a small fraction at lower

Table XI. Comparison of overpotential and effective entropic overpotential at C/1.

Study	Comparison at C/1 discharge at 300 K	
	$I \times \eta$ (mV)	$-TdU/dT$ (mV)
Al Hallaj et al. ⁵⁴	Not calculated	-143 to 26
Al Hallaj et al. ⁵⁵	381 to 1560	-69 to 225
	311 to 756	48 to 294
	276 to 822	
Hong et al. ⁵⁶	(a) 311 to 581	(a) 129 to 225
	(b) 284 to 513	(b) 126 to 252
	(c) 284 to 446	
Bang et al. ⁵⁷	Current not given	-54 to 132
		-15 to 153
Lu and Prakash ⁶¹	Current not given	(a) -84 to 30
		(b) -90 to 48
Lu et al. ⁶²	(a) 31.6 to 191	(a) -18 to 39
	(b) 52.2 to 191	(b) 24 to 45
Luet al. ⁶³	Current not given	-6 to 24
		-84 to 30
		-60 to 90
Lu et al. ⁶⁴	235 to 469	-34 to 66
	213 to 226	-40 to 38
	126 to 150	-23 to 30
Onda et al. ⁶⁵	(a) 189 to 432	(a) 57 to 156
	(b) 230 to 378	(b) 24 to 198
	(c) 203 to 378	
	(d) 203 to 284	
	(a) 450 to 1098	(a) -63 to 243
	(b) 594 to 990	
	(c) 270 to 810	
	(d) 216 to 270	
Onda et al. ⁷¹	(a) Charge: 252 to 504 Discharge: 306 to 576	-6.2 to 197
	(b) Charge: 252 to 306 Discharge: 288 to 630	
	(c) Charge: 270 to 288 Discharge: 270 to 504	
	(d) Charge: 162 to 252 Discharge: 180 to 252	
Thomas et al. ⁷³	Overpotential not given	(a) -30 to 120
		(b) -30 to 66
		(a) -75 to 105
Yang and Prakash ⁶⁹	52.8 to 1050	-6 to 24
	94.9 to 338	-165 to 78
	(a) 37.9 to 471	-54 to 114
	(b) 94.7 to 412	
	(c) 28.4 to 128	
	(d) 150 to 353	

discharge rates. Thus, this observed effect in other studies may simply be an artifact of the testing procedure (i.e., cell cooling). Moreover, the IHC test methods may not be capable of maintaining isothermal conditions during testing due to limited surface heat rejection, which was implied by Lu and Prakash.⁶¹ Also, all of the above conclusions are complicated by the fact that only one investigation has reported the experimental uncertainty for the testing methods (Thomas and Newman: $\pm 2 \mu\text{W}$ with a $\pm 20 \mu\text{W}$ offset). Finally, all of the reported data in the open literature are for relatively small cells (which may not have substantial Joule heating in the current collectors) that will not be used in HEV and EV applications. Clearly, there is an opportunity to develop an improved heat collection method to discern the relative impact of mixing, entropic, overpotential, and current collector resistance heat and to measure heat rates above the nominal C/1 discharge/charge rates, which will be important for designing thermal management systems for lithium-ion battery packs in EVs and HEVs.

From a review of the experimental data, entropic heat should not be neglected in simulation. As shown in Table XI, the product of

temperature and the entropic heat coefficient appears to be of the same order of magnitude as the actual overpotential at the moderately high C/1 rate. This has also been shown in a recently published review paper to be true across a variety of cell chemistries.⁷⁵ In addition, some studies show that the heat rate profile has an S-shaped curve even at the C/1 rate, which can be attributed to entropic heating (e.g., Bang et al.⁵⁷ and Kim et al.⁵⁸).

The measured overall heat generation for these batteries is not large (at most a peak of 84.5 W/L for the 0.92C rate at the end of discharge) in comparison to the power delivered (~ 435 W/L in this case,⁶⁵ with the assumption of a nominal voltage of 4 V). This emphasizes the fact that heat rejection from lithium-ion batteries is not primarily a heat flux issue: it is a low conductivity, high thermal mass problem. In other words, a significant amount of heat is accumulated inside the battery for small temperature rises, but this heat is not easily transported to the surface due to the low effective radial thermal conductivity of the battery. This is clearly demonstrated by Hong et al.,⁵⁶ who noted that the measured thermal energy accumulated inside the cell was approximately equal to one half the estimated heat generated when discharged at the C/1 rate.

Thermal simulation studies.— Several thermal simulations studies have been conducted on lithium-based batteries. The studies listed in Table XII encompass the major investigations on the thermal performance of insertion electrode batteries, which range in scale from single cells to larger spirally wound batteries to full multicell prismatic batteries. These papers can be subdivided into two major categories based on the methodology used to predict heat generation: experimental data or electrochemical models. In this section, the major characteristics of these studies are highlighted, followed by some insights gained from these investigations on both gathering experimental heat generation data and developing appropriate thermal management strategies. In addition, the required thermal properties for battery simulation are also discussed.

Heat generation predictions using experimental data.— In experimental studies, overpotential and entropic heat coefficients gathered from experiments are used to predict the volumetric heat generation rate. As shown in Table XIII, all reviewed simulation studies use the simplified form to predict the heat rate (Eq. 3), which is inserted into the heat equation on a per unit volume basis as follows

$$\rho C_p \frac{\partial T}{\partial t} = \nabla \cdot (k \nabla T) + q''' \quad [11]$$

The first term is the heat stored by the battery, followed by the heat conduction and generation terms. In each study, the battery is divided into multiple cells. Using appropriate boundary and initial conditions, the heat equation is applied to these cells and solved to determine the temperature distribution throughout the battery. The only means of coupling the thermal field to the electrochemical heat generation is through the entropic heat, which is the product of temperature and the entropic heat coefficient.

The thermal simulation studies reviewed here all used direct measurement of the overpotential, and most assume constant and uniform current distribution throughout operation. However, caution must be exercised when collected cell voltage data are used to predict heat generation. For high discharge rates, the battery can heat up substantially, which can allow for a significant cell voltage increase due to the improved electrochemical performance. This can be seen clearly in the experimental data presented by Chen and co-workers^{84,88} for 3C discharge, which shows significant voltage recovery. In contrast, Onda et al.⁷¹ presented a simplified electrochemical model to predict current distribution along their spirally wound cylindrical cell (OD = 18 mm, length = 65 mm). They assumed that current flows only perpendicular to the wind direction and that heat is transported in the radial direction only. Their calculated results show that the temperature difference between the surface and center of the cell was only 1.6°C after 1104 s of discharge at the 3C rate. Their experimental results confirmed that this temperature difference was 1.9°C after 90% discharge. However, no

Table XII. Summary of insertion electrode lithium-battery thermal simulation studies.

Simulation studies on lithium-based batteries	Negative/positive electrode material	Geometry			Heat rate method	
		Wound	Prismatic	Small cell	ECM model	Experimental data
Pals and Newman ⁸³	Li/LiTiS ₂			X	X	
Botte et al. ⁷⁷	C/LiNiO ₂			X	X	
Thomas and Newman ⁴⁹	Li/LiAl _{0.2} Mn _{1.8} O _{4-δ} F _{0.2}			X	X	
Srinivasan and Wang ⁷⁸	C/LiMn ₂ O ₄			X	X	
Smith and Wang ⁷⁹	C/Li(NiCoAl)O ₂ ^a			X	X	
Gomadani et al. ⁸¹	unknown	X			X	
Kumaresan et al. ⁸²	C/LiCoO ₂	X			X	
Pals and Newman ⁷⁶	Li/LiTiS ₂		X		X	
Verbrugge ²⁹	Li/vanadium oxide		X		X	
Song and Evans ⁶⁸	Li/LiMn ₂ O ₄		X		X	
Al Hallaj et al. ²⁸	C/LiCoO ₂	X				X
Chen et al. ⁸⁴	C/LiCoO ₂	X				X
Onda et al. ⁷¹	C/LiCoO ₂	X				X
Chen and Evans ⁸⁵	Li/LiV ₆ O ₁₃		X			X
Chen and Evans ⁸⁶	Li/LiV ₆ O ₁₃		X			X
	Li/LiTiS ₂					
Chen and Evans ⁸⁷	Li/LiTiS ₂		X			X
Chen and Evans ³⁰	C/LiCoO ₂		X			X
Chen et al. ⁸⁸	C/LiCoO ₂		X			X
Kim et al. ^{50,51}	C/LiNiCoMnO ₂		X			X

^a Reference 80.

evidence of current (or SOC) maldistribution was presented. In addition, there may also be substantial resistive heating that arises from current collection in a single battery. As discussed above, the work of Kim et al.,^{50,51} who used a simplified electrochemical parameterization using experimental data, has shown that this resistive heating may be large, even in well distributed batteries.

Heat generation prediction using electrochemical models.—

Detailed electrochemical models have been used to calculate local heat generation in response to temperature changes and vice versa. The studies reviewed here are summarized in Table XIV. A detailed description of electrochemical modeling is outside the scope of this document. An introduction to and details of electrochemical modeling can be found in the chapter on battery modeling in the textbook by Newman and Thomas-Alyea.⁹⁷ The electrochemical models of Doyle et al.,⁹³ Fuller et al.,⁹² Doyle et al.,⁹⁶ and Smith and Wang⁷⁹ are similar. In each of these models, lithium-ion transport through

the electrolyte is modeled using concentrated solution theory in which the driving force for mass transport is the gradient in the electrochemical potential.⁹² Furthermore, the porous insertion electrodes consist of spherical particles with diffusion of lithium ions into the solid. The primary equations in these models are species and charge balances in the electrolyte and solid particles. In addition, Butler–Volmer expressions are used to model the charge transfer kinetics at the solid/electrolyte interface. All of these models are one-dimensional (i.e., current flows only perpendicular to the current collectors), and the primary boundary conditions are as follows:

- No concentration or potential gradients in the electrolyte at the current collector/electrolyte interface
- Lithium concentration symmetry at the center of the spherical particles
- Proportionality between the lithium pore wall flux and the con-

Table XIII. Summary of experimental thermal simulation studies.

Investigation	Heat generation		Cell voltage and OCP	Temperature-dependent parameters
	Equation	Temperature dependency		
Al Hallaj et al. ²⁸	Equation 3	Entropic only	Experimental data in paper	None
Chen et al. ⁸⁴	Equation 3	Entropic only	Experimental data in paper	Surface convection
Onda et al. ⁷¹	Equation 3	Entropic heat and current distribution	Experimental data in paper	Heat capacity, surface convection
Chen and Evans ⁸⁵	Equation 3	Entropic only	Hooper and North ⁸⁹	None
Chen and Evans ⁸⁶	Equation 3	Entropic only	LiV ₆ O ₁₃ : Hooper and North ⁸⁹ LiTiS ₂ : Gauthier et al. ⁹⁰	None
Chen and Evans ⁸⁷	Equation 3	Entropic only	Gauthier et al. ⁹⁰	None
Chen and Evans ³⁰	Equation 3	Entropic only	Au and Sulkes ⁹¹ (discharge) Fuller et al. ⁹² (OCP)	None
Chen et al. ⁸⁸	Equation 3	Entropic only	Experimental data in paper	Surface convection
Kim et al. ^{50,51}	Equation 7	Entropic only	Curve fit to experimental data	None

Table XIV. Summary of thermal simulations studies using electrochemical models to predict heat generation.

Investigation	Electrochemical model	Heat generation		OCP	Operation type
		Equation	Temperature dependency		
Pals and Newman ^{76,83} Botte et al. ⁷⁷	Doyle et al. ⁹³ Fuller et al. ⁹²	Equation 3 Rao and Newman Equation 4 plus negative electrode decomposition equation 17	Overpotential Decomposition reaction rate	Not given Dahn et al. ⁹⁴ Doyle ⁹⁵	Constant <i>I</i> Constant <i>I</i>
Thomas and Newman ⁴⁹	Doyle et al. ⁹³	Given formulation with or without mixing or reaction heat	Overpotential and entropic, but simulations are isothermal	Thomas et al. ⁷³	Constant <i>I</i>
Srinivasan and Wang ⁷⁸	Doyle et al. ⁹⁶	Gu and Wang ⁴⁶	Overpotential and entropic	Doyle et al. ⁹⁶	Constant <i>I</i>
Smith and Wang ⁷⁹	1D model in paper	Given formulation: integrate overpotential, ohmic heat in matrix and electrolyte, contact resistance at collector	Overpotential and ohmic	Equations in paper	Constant <i>I</i>
Gomadam et al. ⁸¹	Doyle et al. ⁹³	Gu and Wang ⁴⁶	Overpotential, ohmic, and entropic	Not given	Constant <i>I</i>
Kumaresan et al. ⁸²	Doyle et al. ⁹³	Gu and Wang ⁴⁶	Overpotential, ohmic, and entropic	Measured in paper	Constant <i>I</i>
Verbrugge ²⁹	Applied voltage use to solve for <i>I</i> and <i>T</i> fields	Equation 3	Overpotential, ohmic, and entropic	Data given in Paper	Constant <i>V</i>
Song and Evans ⁶⁸	Doyle et al. ⁹³	Given formula in Paper includes activation/concentration overpotential in the electrolyte and positive electrode, ohmic drop across SEI, electrolyte, and electrode	Overpotential, ohmic, and entropic	Doyle et al. ⁹³	Constant <i>I</i>

centration gradient at the solid particle surface through the solid diffusion coefficient

- No potential gradients in the solid matrix at the separator/electrode interface⁷⁹
- Applied constant current discharge

Other expressions are required to close the system of equations: Faraday's law relating electrolyte current to pore wall flux,^{92,93,96} conservation of current density in the two phases,^{92,93,96} and values for the SEI resistance (included in Butler–Volmer kinetics expression).⁷⁹ These models allow determination of the local potential and reaction current density variation in the stack thickness for a fixed total current. The operation of the cell can be sensitive to temperature variations due to its influence on various transport properties in the battery. As shown in Table XV, the primary temperature-dependent transport properties are electrolyte ionic conductivity and diffusion coefficient and solid electronic conductivity and diffusion coefficient. Other possible temperature-dependent properties include the transference number⁷⁷ and the mean molar activity coefficient (affects the current–potential relationship).⁸²

In the model by Verbrugge,²⁹ current is generated in each subdivided battery section using a relationship between the applied cell voltage and the composite charge conductivity of the entire cell (see Eq. 1). The composite charge conductivity is calculated as follows

$$\sigma_x = \left(\frac{l_a}{\sigma_a} + \frac{l_c}{\sigma_c} + \frac{l_e}{\sigma_e} + \frac{RT}{i_{o,a}nF} + \frac{RT}{i_{o,c}nF} \right)^{-1} \quad [12]$$

The ionic conductivities of both the electrode and the electrolyte are calculated as follows

$$\sigma_{\text{electrode}} = \frac{k}{N_L T} \quad [13]$$

$$\sigma_e = A_o \exp\left(-\frac{E_A}{RT}\right) \quad [14]$$

The interfacial resistance is modeled using the exchange current density at each electrode, which is assumed to follow an approximate temperature-dependent relationship

$$i_o = A_{i_o} \exp\left(-\frac{\Delta H_o}{RT}\right) \quad [15]$$

The exchange current density multiplier (A_{i_o}) is used as an adjustable parameter in the model. For his simulation, Verbrugge²⁹ solved the coupled electrochemical and thermal fields simultaneously for a fixed SOC and applied voltage for a bipolar battery stack. Portions of the cell that are more insulated from the environment rise in temperature, thus allowing more current to pass. This increases the local heat generation rate and thus further increases the temperature of these internal cells.

A description of the form of the heat generation equation for each of these studies is listed in Table XIV. Pals and Newman^{76,83} and Verbrugge²⁹ apply the simplest form to calculate heat generation rate (Eq. 3) using the average cell overpotential, whereas the other methods take advantage of the detailed electrochemical information to use variations of the expressions presented by Gu and Wang,⁴⁶ Rao and Newman,⁴⁸ or Thomas and Newman.⁴⁹ Smith and Wang⁷⁹ integrate the local reaction and ohmic overpotentials to estimate the heat rate. They also introduce a contact resistance between the current collectors and the electrodes, which is modeled as follows

$$q = I^2 \frac{R_f}{A_{\text{electrode}}} \quad [16]$$

This resistance R_f is an empirical parameter for which Smith and Wang⁷⁹ assume a constant value of 20 $\Omega \text{ cm}^2$, which dominates other heat generation mechanisms. Other parameters can also be

Table XV. Summary of temperature dependency in electrochemical model-based thermal simulation studies.

Investigation	Temperature-dependent parameters	Current/temperature feedback simulated?
Pals and Newman ^{76,83}	Electrolyte ionic conductivity and diffusion coefficient	No—although transport properties are temperature dependent, feedback is on the potential only
Botte et al. ⁷⁷	Ion diffusion coefficients in the solvent, transference number, solid diffusion coefficients, ionic conductivity of electrolyte	No—transport properties are evaluated at 25°C only
Thomas and Newman ⁴⁹	None given	No—simulation was isothermal
Srinivasan and Wang ⁷⁸	All diffusion coefficients and conductivities	Yes—galvanostatic, but reaction distribution is temperature dependent
Smith and Wang ⁷⁹	Solid and electrolyte diffusion coefficients, electrolyte conductivity	No—simulations are isothermal
Gomadam et al. ⁸¹	Same as Pals and Newman ⁷⁶	Yes—galvanostatic, but reaction distribution is temperature dependent
Kumaresan et al. ⁸²	Solid-phase diffusion coefficient for negative electrode, mean molar activity, coefficient of the salt, ionic conductivity and salt-diffusion coefficient of the electrolyte	No—temperature dependent properties cause voltage changes, not current distribution
Verbrugge ²⁹	Interfacial exchange current density coefficient, ionic conductivity of the electrolyte, thermal conductivity of the electrodes and electrolyte, heat capacity of electrodes	Yes
Song and Evans ⁶⁸	Ionic conductivity and diffusion coefficient of electrolyte	No—voltage profile was modified for fixed current density

included in the heat generation equation, including the temperature-dependent expression for heat generated due to side reactions (e.g., decomposition of the negative electrode⁷⁷)

$$q_{\text{reaction}} = -\Delta H_{\text{rxn}} \times \text{Rate}_{\text{rxn}} \quad [17]$$

In all cases, the temperature dependency of the electrochemical performance is directly coupled to the thermal model through these expressions for the volumetric heat generation, which represents a significant difference from the majority of experimentally based thermal simulations. However, only a few of these studies (Srinivasan and Wang,⁷⁸ Gomadam et al.,⁸¹ and Verbrugge²⁹) allow the current distribution inside a battery to vary with temperature (see Table XV).

Battery thermal properties.—The thermal properties of batteries exhibit interesting characteristics. The battery is a layered cell containing multiple materials with different thicknesses and thermal properties (see Fig. 2). As a result, the thermal conductivity of the battery is anisotropic. Heat flowing perpendicular to the wound direction must flow through each sheet in series, while heat flowing

along the stack flows through each layer in parallel. Because the thickness of each layer is very small, significant computational time is consumed when attempting to resolve heat flowing in each layer. Instead, the battery unit cell is typically modeled as a uniform layer with anisotropic thermal conductivity (and uniform heat generation) as follows

$$k = \frac{\sum k_i t_i}{\sum t_i} \quad [18]$$

$$k_{\perp} = \frac{\sum t_i}{\sum \frac{t_i}{k_i}} \quad [19]$$

Chen et al.⁸⁴ presented an example double-coated unit cell with double-coated current collectors. Using the reported data in Table XVI, the parallel and perpendicular thermal conductivities are 33.9

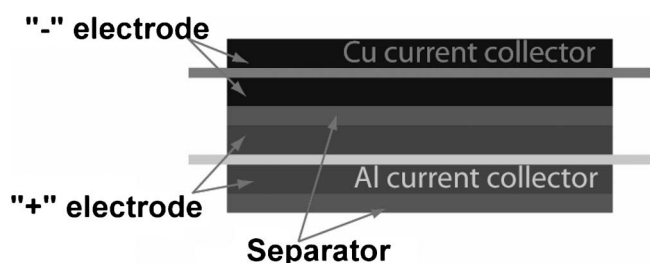


Figure 2. Diagram of a spirally wound battery unit cell for a lithium-ion battery.

Table XVI. Example unit cell dimensions and properties from Chen et al.⁸⁴

Layer	t (μm)	ρ (kg/m^3)	C_p [$\text{J}/(\text{kg K})$]	k [$\text{W}/(\text{m K})$]
Coated carbon negative electrode	55	1347	1437	1.04
Cu current collector	14	8933	385	398
Electrolyte soaked separator	30	1008	1978	0.334
Coated LiCoO ₂ positive electrode	55	2328	1269	1.58
Al current collector	20	2702	903	238

and 0.885 W/(m K), respectively. The substantially lower perpendicular thermal conductivity is primarily due to the electrolyte-soaked separator and the electrodes, which govern the heat transport from the battery. The heat capacity for the equivalent cell is volume-averaged as follows

$$\rho C_p = \frac{\sum (\rho C_p)_i t_i}{\sum t_i} \quad [20]$$

Using the same data in Table XVI, the heat capacity for this lithium-ion cell is 2404 kJ/(m³ K). This method has been shown to give results similar to those obtained from calculating the contribution from each layer separately.⁸⁵ In general, these bulk properties are assumed temperature independent in the simulation studies.

One interesting note about the literature-reported values is that their appears to be only one study (Maleki et al.⁹⁸) that reports the technique used to measure the necessary thermal properties in sufficient detail. The remainder of investigations simply report the thermal properties used. In their study, Maleki et al. measured the composite thermal conductivity (in stack parallel and perpendicular directions) and specific heat of the negative and positive electrodes (C/LiCoO₂ with thickness of 0.198 and 0.186 mm, respectively) and of a three layer stack consisting of the negative electrode, plastic separator, and positive electrode both with and without an electrolyte [1 M LiPF₆ in EC-DMC (dimethyl carbonate) in 1:1 wt %] using a xenon flash technique. The tests were conducted at two thermodynamic open circuit potentials (2.45 and 3.75 V) to elucidate any effects of SOC on the measured thermal properties. The thermal conductivity in the perpendicular to the stack was estimated to be 3.40 W/(m K) irrespective of the SOC. However, there appears to be something incorrect with this measurement technique for estimating the thermal conductivity perpendicular to the stack, which is critical for designing thermal management systems. For example, the thermal conductivities at 3.75 V for the positive and negative electrodes are 2.49 and 1.20 W/(m K) (possibly without an electrolyte), respectively, but the composite thermal conductivities for a negative electrode/separator/positive electrode assembly without and with an electrolyte are 2.36 and 3.40 W/(m K), respectively. Neither of these values is mathematically possible: just these two layers by themselves would produce an effective thermal conductivity of 1.704 W/(m K) using Eq. 19. Furthermore, the thermal conductivity of a polypropylene separator should be between 0.15 and 0.17 W/(m K),⁹⁹ and the electrolyte conductivity should be similar [e.g., the thermal conductivity of DMC is near 0.16 W/(m K) (Ref. 100)]. In addition, their stack assembly is incomplete for an actual battery because an additional separator is required for a double-side coated current collector (see Fig. 2). However, because the addition of the electrolyte does appear to have a significant effect on the measured conductivity, there must be significant thermal contact resistances between the separator and the electrodes and possibly between the electrode material and the current collectors. This investigation was done with special fixtures that ensured adequate contact pressure during the tests. In actual cells, the contact pressure may not be the same, and further investigation is warranted. In addition, there have been no reported values for the LiFePO₄ positive electrode (although recently Guo et al.¹⁰¹ cite 1.48 W/(m K), but no explicit reference was given), which is known to be a poor electrical conductor requiring special processing techniques for use in commercial batteries.¹⁰² Thus, there appears to be a significant need to understand the thermal conductivity of assembled cells.

Analysis of thermal simulation studies.— This section summarizes observations and conclusions made from the thermal simulation studies on batteries with lithium-based insertion electrodes presented above. Because these models provide insights into battery performance, the focus here is on implications for measuring battery heat generation and impacts on thermal management strategies.

The investigations that calculate heat generation using experimental polarization data use only one temperature during their experiment. However, as shown in the simulation studies that use electrochemical models, that assumption may not hold while the battery is operating because at higher temperatures, the battery operates at a lower polarization due to increased efficiency. For example, in their single-cell study on a titanium disulfide polymer electrolyte cell, Pals and Newman⁸³ showed that the polarization curves are a strong function of temperature. As the temperature increases, both the ionic conductivity and the diffusion coefficient in the electrolyte increase and improve the lithium-ion mass transport, thus allowing the cell to operate more efficiently, generating less heat. At high discharge rates (4 mA/cm² and higher for a 90°C initial battery temperature) and adiabatic operation, their cell potential reached a local minima near the beginning of discharge because increased cell temperatures offset cell polarization. For the highest discharge rate studied (6.4 mA/cm²), the cell potential drops almost to the cutoff potential (1.7 V) prior to rebounding. This explains the unusual voltage-SOC data for 3C discharge reported by Chen et al.⁸⁴ For discharge with heat transfer, Pals and Newman showed that the temperature decreased as the rate of convection increased. This causes the cell potential to decrease and, therefore, heat generation rate to increase. Similarly, Srinivasan and Wang⁷⁸ showed that for a C/LiMn₂O₄ system, the rate of heat generation is higher at lower discharge rates for an isothermal cell than for a cell that accumulates heat adiabatically or with heat transfer to the environment. Again, this is because the cell operated adiabatically or with heat rejection undergoes an increase in temperature as it discharges, thus operating more efficiently than for isothermal operation. Because it is a strong function of temperature, more studies measuring the heat generation rate should be conducted. Furthermore, these temperature-dependent measurements should be incorporated into the simplified simulations that use experimental data.

There also appears to be disagreement between simulated and experimental results, especially at higher discharge rates. Al Hallaj et al.²⁸ reported that their experimentally based predictions on a C/LiCoO₂ 18650 cell (1.35 Ah) simulate the cell surface temperature for discharge rates below C/1. However, at the C/1 rate, the temperature rise is not predicted well. Although essentially the same at the end, they underpredict the cell temperature by about 2.9°C when the cell is about halfway discharged. This is significant because the total temperature rise is 12.1°C. In addition, although they predicted that the cell would rise 57.4°C for a 2C discharge, because they poorly predicted the C/1 rate, this estimate should be used with caution. Song and Evans⁶⁸ showed that their detailed electrochemical-thermal model did not predict high rate discharge heat generation for a 0.6 mAh Li/LiMn₂O₄ coin cell: both path and magnitude are off considerably, as much as 19% underpredicted at the end of discharge. In the study summarized by Gomadam et al.⁸¹ on the 18650 cell, the overall trend of temperature for discharge rates ranging from 10 to 60 A/m² is predicted reasonably well but the shape of the simulated curve is different from the collected experimental data. In the study by Thomas and Newman⁴⁹ on a Li/LiAl_{0.2}Mn_{1.8}O_{4.8}F_{0.2} coin cell, the complex heat profile, which is very dependent on the entropic heat, is captured fairly well for the C/8 and C/3 discharge and charge rates using their detailed isothermal electrochemical model, even though there is as much as 50% overprediction in some stages. In contrast, the 2C 5 min discharge and charge heat generation is consistently overpredicted, by as much as 67%. In the study by Onda et al.⁷¹ on a 1.80 Ah C/LiCoO₂ 18650 cell, there are discrepancies in the surface temperature predictions, especially at the end of charge or discharge. For discharge, the 1C and 2C temperatures at 0.2 SOC are underpredicted by 2.8 and 1.9°C, respectively, while the 3C temperature is overpredicted by 5°C at the same discharged state. (The temperature rises for the 1C, 2C, and 3C discharge rates are 23.1, 43.8, and 67.5°C, respectively.) For charge, the 1C rate data are underpredicted by 2.2°C (at a total temperature rise of 9.2°C). However, the 1.5C charge data are pre-

dicted very well, but this is probably an artifact of the short duration—only 0.1 Δ SOC is possible prior to reaching the cutoff voltage.

In the few studies where comparison is possible, the simulated heat generation rates also appear to be inconsistent with the measured rates. The following studies examined the 1.35 Ah C/LiCoO₂ Sony 18650 cell: Al Hallaj et al.,²⁸ Chen and Evans,³⁰ Hong et al.,⁵⁶ and Al Hallaj et al.⁵⁵ The simulation results for the C/1 discharge from Al Hallaj et al.²⁸ show that the volumetric heat generation rate varied from 27 to 59 W/L, with most of the data (i.e., from 0.1 to 0.7 DOD) falling in the range from 30 to 45 W/L. Similarly, the expected heat generation rates at a C/0.9 discharge rate for a similar cell reported in Chen and Evans³⁰ use only the overpotential data range from 20 to 40 W/L, with the majority of rates near 30 W/L. In contrast, the experimental studies of Al Hallaj et al.⁵⁵ and Hong et al.⁵⁶ show that for the same 1.35 Ah Sony 18650 cell, the heat rate increases linearly from 0 to 27.9 W/L and from 0 to 33.3 W/L, respectively. This difference in magnitude between the experimental and simulation studies can be explained if the volumes used by the reviewers were incorrectly estimated. However, this does not account for the significant difference in observed trends, even for the same battery brand, size, and chemistry. Additional comparisons across various studies could be made if the simulation studies reported volumetric heat generation rate (e.g., Srinivasan and Wang⁷⁸ and Botte et al.⁷⁷) and if a wider range of currents were tested for various experimental studies (e.g., Kobayashi et al.⁵⁹).

In summary, simulation results do not adequately predict the trend of heat generation reported by various experiments, which manifests itself in incorrectly predicting the temperature rise. Some of the discrepancies may be attributable to differences in the battery design and the simulations could be considered adequate, but the experimental methods mostly do not report enough key parameters to enable assessment, often do not adequately control relevant parameters while others are varied, do not address wide enough ranges of discharge rates, times, and other parameters, do not measure internal temperatures in batteries with acceptable spatial and temporal resolution, and do not report measurement uncertainties. Therefore, it is difficult to gauge the adequacy of the models on the one hand and also the accuracy of the measurements on the other hand.

It was stated above that internal portions of large batteries poorly transport heat to the cooling media. For low surface convection, this results in increased overall temperatures for the more thermally insulated internal portions of the battery. Furthermore, increasing the surface convection can mitigate the peak temperature rise, but does so at the expense of producing a substantial thermal gradient. For example, using a 2D simulation, Chen and Evans⁸⁶ showed that for C/0.3 discharge in a 5.0 cm long by 20 cm thick LiV₆O₁₃ polymer battery, as the surface convection increased from 6 to 25 W/(m² K), the peak temperature decreased from 122 to 116°C, but the thermal gradient increased from 8 to 26°C. Similar results were shown for their subsequent lithium-ion battery study:³⁰ an increase in temperature difference from 2 to 17°C for a surface convection increase from 6 to 25 W/(m² K). The thermal gradients were greatest in the cell stack direction due to the low conductivity polymer electrolyte [e.g., 0.16 W/(m K)] and separator [0.83 W/(m K)]. Al Hallaj et al.²⁸ also obtained similar results on a 18650 lithium-ion cell discharge at the C/1 rate. For an applied surface convection of 1 W/(m² K), the peak temperature of the battery rose more than 80°C at the end of discharge, but with almost no difference inside the battery. In contrast, the battery peak temperature rose almost 20°C for an applied surface convection of 100 W/(m² K), while a 7.5°C thermal gradient was induced.

As mentioned above, the cell operating temperature affects the performance of the cell by improving its electrochemical performance. Parts of batteries in closer thermal proximity to the cooling environment will generate more heat than insulated interior parts of the battery when current is uniformly distributed across the battery. As a result, the colder cells that generate more heat flatten the tem-

perature gradient inside the battery. This is clearly shown by the works of Pals and Newman⁷⁶ and Song and Evans.⁶⁸ Pals and Newman simulated the temperature response of a multicell prismatic lithium–titanium disulfide polymer electrolyte battery using time–temperature lookup tables for heat generation produced by their previous single-cell isothermal model.⁸³ This allowed for each cell to generate heat, depending only on its temperature and discharged state (which was uniformly applied). For the 576 cell stack discharged at the C/3 rate, the temperature and heat generation was essentially uniform throughout the first 25 min of discharge. At the end of discharge, the heat generation rate at the cooler cells was more than 2 times higher than in the warmer interior cells. This phenomenon tended to flatten out the temperature profile. Song and Evans⁶⁸ compared a coupled electrochemical–thermal model to a decoupled thermal model for a multicell Li/LiMn₂O₄ 10 cm × 10 cm polymer battery. The thermal model showed a roughly parabolic temperature profile at the end of a 0.5 mA/cm² discharge with a 15°C temperature gradient. The coupled model showed a slight decrease in the temperature gradient to 13°C, but the interior cell temperature profile was flatter.

Colder cells will generate more heat than warmer cells for the same applied current. However, the cell performance increases at higher temperatures due to improved mass transport. For a larger battery, this allows additional current to pass through hotter sections of the battery, thus counteracting increased polarization for colder cells. This is clearly shown by the work of Verbrugge,²⁹ who presented a 3D coupled electrochemical–thermal mode for a lithium vanadium oxide polymer electrolyte bipolar battery. The battery contained 35 parallel modules, with each module containing 35 cells. Each cell in the module was 56.5 cm × 20.3 cm in cross section, and the total depth of the module was 30 cm. As mentioned above, the composite conductivity increases with temperature. Hence, the cooler cells allow less current to pass for the same voltage. For example, the locations at the center of the cell can be more than 20°C higher than at the cooled edges after 30 min of discharge at an applied voltage of 2.63 V for each cell (2.7 V was the OCP). This resulted in a doubling of the current passing through the center cells versus the surface cells (~30 vs ~15 mA/cm²). In another study, Gomadam et al.⁸¹ summarized a previous investigation on lithium-ion 18650 cells and noted that for a cell cooled preferentially at the bottom opposite the cell terminals, more current passes through the top of the cell because the colder cells have become more resistive. However, as pointed out by Kim et al.,^{50,51} there appears to be a significant link between the current field and the local heat generation. In their simulation, the simplified electrochemical model had no temperature feedback. Thus, the current field was entirely dependent on the design of the current collectors. In light of the simulations by Verbrugge, Srinivasan and Wang, and Pals and Newman showing the coupled nature of temperature and local current generation, it would be best that their electrochemical model be modified to further elucidate the impact of temperature on the local cell performance. This is apparently what is being currently investigated at the NREL.^{52,53}

Several investigations show that as the discharge rate increases, the cell temperature at the end of discharge reaches a maximum, followed by a subsequent decrease. With a fixed cutoff potential, the discharge time decreases faster than the heat generation rate as the applied current increases. Botte et al.⁷⁷ investigated the impact of increased discharge rate on the peak cell temperature for a C/LiNiO₂ lithium-ion cell using a detailed electrochemical model. For rates higher than C/0.2, the time elapsed before the cell reached the cutoff potential decreased enough to limit the temperature rise. For example, the elapsed time for a discharge rate of C/0.1 was 1/6 of that for C/0.2, thus reducing the temperature rise from 42°C at C/0.2 to 22°C at C/0.1. Therefore, as the rate was increased, the peak temperature achieved by the cell decreased despite an increase in the heating rate. Srinivasan and Wang⁷⁸ also showed that as the discharge rate increased, the total heat energy peaked and subsequently decreased at higher rates. The peak occurs because at high

Table XVII. Summary of entropic heat coefficients used in the reviewed thermal simulation studies.

Investigation	Entropic heat coefficient
Pals and Newman ^{76,83}	Neglected
Botte et al. ⁷⁷	Neglected
Thomas and Newman ⁴⁹	Function of SOC in Thomas et al. ⁷³
Srinivasan and Wang ⁷⁸	Function of SOC using Thomas et al. ⁷³ and Al Hallaj et al. ⁵⁴
Smith and Wang ⁷⁹	Neglected
Gomadam et al. ⁸¹	Not mentioned, but included in heat generation formulation
Kumaresan et al. ⁸²	Thomas and Newman ⁷²
Verbrugge ²⁹	Not given, but could be determined from data in Paper
Song and Evans ⁶⁸	−1.1 mV/K
Al Hallaj et al. ²⁸	Linear fit between 4.044 and 3.227 V: −0.419 to −0.753 mV/K
Chen et al. ⁸⁴	−22.0 mV/K
Onda et al. ⁷¹	Function of SOC: −0.66 to 0.022 mV/K
Chen and Evans ⁸⁵	0.22 mV/K
Chen and Evans ⁸⁶	0.22 mV/K
Chen and Evans ⁸⁷	−0.237 mV/K
Chen and Evans ³⁰	−0.414 mV/K
Chen et al. ⁸⁸	0.22 mV/K
Kim et al. ^{50,51}	Not given

rates, cell utilization decreased. This was further substantiated by observing that the reversible heat, which was directly linked to the amount of reaction, decreased for higher discharge rates. For example, if the discharge rate increases from $C/0.5$ to $C/0.33$, the cell utilization drops quickly from 80 to 36%. This caused a reduction in the total amount of energy generated from 3.5 to 2.1 kJ. However, if a battery is cycled repeatedly, as in an HEV application, without adequately removing the accumulated heat, the cell temperature can continue to rise. For example, Chen and Evans³⁰ simulated ten repeated cycles of constant current discharge ($C/0.91$) and constant current, constant voltage charge ($C/0.61$, unknown voltage) for a 20 cm lithium-ion battery cube. The results showed that the temperature increased to a maximum of 80°C and the thermal gradient increased to 12.5°C.

From the simulation studies, it is clear that the thermal management strategies will significantly impact the performance of batteries. The negative feedback produced by colder cells generating more heat should tend to stabilize temperature maldistribution inside the battery. Conversely, the positive feedback produced by hotter cells generating more current (and thus heat) will exacerbate inherent temperature gradients generated from uneven cooling, which will be more pronounced for multiple cells connected in parallel instead of in series, where all current must pass through each cell. The more serious consequences of the current/temperature positive feedback are the increased chances of thermal runaway stemming from overcharge, overdischarge, or dangerously high temperatures (e.g., separator melting temperatures) resulting from repeated, rapid cycling or extreme environments. Thus, it is imperative that the cooling strategies cool the battery uniformly and mitigate thermal accumulation by decreasing the thermal resistance between the hotter cells of the battery and the cooling media.

Another observation is that the entropic heat is applied inconsistently to the thermal models. Table XVII shows the entropic heat coefficients used in the simulation studies reviewed here. In these studies, the entropic heat is neglected,^{76,77,79,83} assumed constant,^{30,68,84-88} assumed linear between two SOC measurements,²⁸ a nonlinear function of SOC,^{49,71,78,82} and not reported.^{29,50,51,81} As the previous section on experimental methods

for reversible heat measurement shows, the entropic heat can be of the same order of magnitude as the reversible heat, which is consistent with the reported values in the thermal simulation studies. (One exception is the study of Chen et al.,⁸⁴ which reports an entropic heat coefficient of −22.0 mV/K. This is probably a misprint since they referred to the study of Chen and Evans⁸⁵ for this value.) Smith and Wang⁷⁹ argued that for HEV applications, the battery cycles around a specific SOC and that the reversible nature of the entropic heat should cancel when cycled repeatedly. However, because the maximum entropic heat may not occur when the overpotential heat is at a maximum, the impact of the reversible heat is not straightforward. Thus, because the entropic heat is significant, even at moderately high charge and discharge rates, it is best to include entropic heating as a function of SOC in all thermal simulations.

Existing Thermal Management Strategies

Although obviously an important topic for various battery applications, there are very few studies conducting detailed investigations of battery thermal management strategies. This section reviews some of the thermal management techniques used in commercial HEVs and reported elsewhere in the literature.

The 2000 Honda Insight and 2001 Toyota Prius were the first commercially available hybrid electric vehicles, and the NREL has conducted a series of thermal performance tests on these battery packs both inside¹⁰³ and outside^{40,104} the vehicle. Both vehicles use multiple nickel-metal hydride batteries to recover and supply energy from and to the vehicle drivetrain. Both battery packs also contain multiple 7.2 V modules of six batteries, also connected in series. The Prius pack is larger (38 modules, 273.6 V, 1.78 kWh) and the batteries are prismatic, while the Insight pack (20 modules, 144 V, 0.94 kWh) uses cylindrical D-sized batteries. The battery packs are both cooled using conditioned air taken from the cabin and exhausted to the ambient, and each pack contains special features to mitigate temperature maldistribution among cells. In the Prius pack, air flow is divided in parallel between each of the modules, each arranged with decreasing space between each module from the air inlet. This is an attempt to distribute the air more evenly across the pack. For the Insight pack, the six batteries in a module are stacked onto one another, making a single column. The 20 modules are arranged in three rows of 6, 7, and 7 modules, similar to an aligned tube-bank. Air is drawn through the aligned bank across the three rows in parallel. Special baffles designed to decrease airflow maldistribution hold the batteries in place and direct the air over the tubes. The first modules in each row are covered with a plastic sleeve, which is designed to increase the thermal resistance between these batteries and the cold air inlet stream.

In their first investigation, Zolot et al.⁴⁰ instrumented the Insight pack with a set of thermocouples to monitor its response during in-vehicle dynamometer testing using the US06 standard driving cycle at three different ambient soak temperatures (without cabin conditioning): 0, 25, and 45°C. In the three tests, the hottest cells are near the air inlet, which is caused by insulating the first column of modules, and they commented that, generally, the temperature differential across the pack approached 3–4°C. It is interesting to note that the delivered pack power reach at least ± 5 kW about 20 times during each of the tests, corresponding to a rate of 5.34C.

Zolot et al.¹⁰⁴ presented results from out-of-vehicle testing on the Prius using power profiles generated by ADVISOR vehicle simulation software for the US06 drive cycle. To thermally manage the pack, air is drawn from the cabin using a 12 V blower that operates at three different nominal speeds. The speed is selected based on the temperature of the pack, determined from a thermal well temperature sensor. During testing, the investigators instrumented all 38 channels with thermocouples. The pack was placed in a controlled environmental chamber while undergoing testing. The test consisted of 12 consecutive 20 min US06 power profile cycles at different ambient temperatures (0, 25, and 40°C). In this test, the observed thermal gradient was dependent on the blower speed but generally was around 4–5°C. However, for the tests at 0°C, the blower does

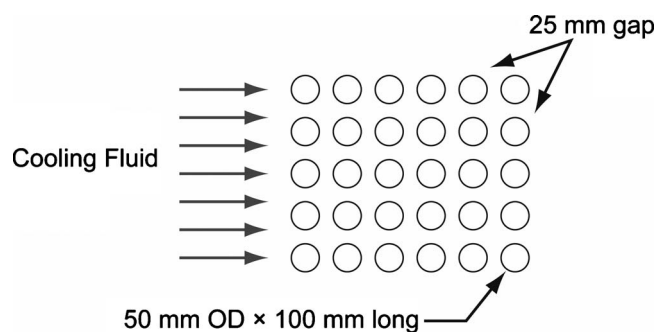


Figure 3. Sample battery thermal management system used for comparing air and liquid cooling systems.

not turn on for approximately 80 min, causing the temperature gradient across the pack to increase up to 11.4°C , with a peak temperature of 39.1°C . After the blower turns on, the pack begins to cool and continues cooling throughout the remainder of the cycles, which decreases the maximum temperature differential to $\sim 8.3^{\circ}\text{C}$. In addition to the US06 tests, Zolot et al.¹⁰⁴ attempted to cycle the battery using an aggressive sport utility vehicle 25 min test. However, this test could not be continuously repeated at 25°C because the peak temperature of the pack reached unsafe limits (55°C) during the second cycle. They suggested that this cycle causes large amounts of internal heat generation (27.84 W/module).

In the tests conducted on the Insight and Prius battery packs, only the surface temperature was monitored in a few discrete locations inside the pack. Hence, the true maximum temperature differential is not known. However, it is clear that if one wishes to maintain fine temperature uniformity for lithium-ion battery packs (which have more inherent safety risks than nickel-metal hydride packs), air may not be the best heat transfer medium. Hence, due to their larger specific heats and densities, liquids may improve both the cell-to-cell temperature gradients and maximum temperature rise. (However, care must be taken using ionically conductive fluids. For example, water decomposes above 1 V, producing hydrogen gas when in contact with both electrodes of the battery.) This can be demonstrated using the following sample calculation. Figure 3 shows a simple arrangement of five rows of six 50 mm OD and 100 mm long (into the page) example batteries spaced 25 mm apart in the transverse and longitudinal directions. Each of these batteries are assumed to generate 30 W/L of heat, which is similar to the rate published by Al Hallaj et al.²⁸ for $C/1$ discharge (i.e., 1.35 A) at an open circuit potential of 3.5 V, which, for an 18650 cell (i.e., 16.54 mL), results in the nominal power output of 285.7 W/L . Hence, each battery (internal volume is 0.196 L) generates 5.89 W of heat and 56.1 W of power. The batteries in each row are cooled in a series fashion, and, assuming steady state, can be modeled as an aligned tube-bank using the Zhukauskas¹⁰⁵ correlation documented in Incropera and DeWitt.¹⁰⁶

Assuming a Reynolds number of 20,000 and an inlet temperature of 25°C , an air volumetric flow rate of $288.9\text{ m}^3/\text{h}$ across the tube-bank would produce 42.9 Pa of pressure drop, resulting in an ideal pumping power of 3.4 W. For this flow rate, the air temperature difference from inlet to outlet would be 1.87°C . In contrast, water flowing at 25°C at a Reynolds number of only 200 (i.e., 2.68 liters per minute) produces a pressure drop of 19.1 mPa, resulting in an ideal pump power requirement of only $0.86\text{ }\mu\text{W}$. Furthermore, due to the increased density (997.1 vs 1.169 kg/m^3) and specific heat [4.183 vs 1.007 kJ/(kg K)], the water thermal capacity rate is much higher than for air (186 vs 94.3 W/K), which results in only a 0.95°C rise across the six rows. This, however, is only one advantage of liquid cooling; due to the poor heat transfer characteristics of air, the battery surface temperature will be lower for the liquid cooling. The air-side heat transfer coefficient in this illustration is

$59\text{ W/(m}^2\text{ K)}$, whereas the liquid heat transfer coefficient is larger: $180\text{ W/(m}^2\text{ K)}$. This causes the steady-state temperature at the battery surface to be 6.32°C higher than the air temperature, but only 2.09°C for water for equal dissipation rates. This results in a maximum temperature rise of 8.19 and 3.04°C from the cooling fluid inlet temperature for the air-cooled and water-cooled systems, respectively. The difference in temperature rise between the two methods exists in spite of the Reynolds number and pumping power being several orders of magnitude lower for water than for air.

These values scale with the heat generation rate, and the corresponding difference between the two methods would be substantially greater for increased heating rates. Furthermore, fluid maldistribution would have a greater impact on this temperature difference for the air-flow system due to its lower specific heat and thermal conductivity. For example, if the flow is halved (to a Reynolds number of 10,000 for air and 100 for water), the inlet-to-outlet temperature difference increases from 1.92 to 3.75°C for the air-cooled system whereas it increases from 0.95 to 1.90°C for the water-cooled system. Due to the reduced heat transfer coefficient, the temperature difference between the bulk fluid temperature and the surface is even greater: from 6.32 to 9.78°C for air and from 2.09 to 2.88°C for water. It should be emphasized that these calculations are only for steady-state operation, which may not occur in practice due to the transient nature of both the HEV driving cycle and the heat generation rate. Nonetheless, it is clear that a liquid-cooled system will still be better at minimizing the peak temperature rise due to its much higher heat transfer coefficient.

As an alternative to direct liquid or air cooling, researchers at Illinois Institute of Technology¹⁰⁷⁻¹¹⁰ have proposed placing the battery module in a liquid/solid phase change material (PCM) to promote cell-to-cell temperature uniformity. Khateeb et al.¹⁰⁹ present a simulation of a lithium-ion battery pack intended to replace a lead-acid battery pack for an electric scooter. The lead-acid battery is nominally 12 V, with average and peak current ratings of 18–24 and 55 A (for 300 ms), respectively. The replacement battery consists of 2 modules of 18 18650 lithium-ion cells, each rated at 3.67 V and 2.0 Ah. There are six parallel groups of 3 cells in series, resulting in a nominal voltage and capacity of 11.1 V and 12 Ah, respectively, per module. The PCM is a paraffin wax with a melting temperature range of 40 – 44°C and a latent heat of melting/solidification of 195 kJ/kg . The wax fills the voids in between the cells and has solid and liquid phase densities of 822 and 910 kg/m^3 . Heat generated by the battery is first rejected to the PCM and then to the battery case, which is in contact with ambient air. The investigators assume 5 and $20\text{ W/(m}^2\text{ K)}$ convection coefficients on the battery case surface while the scooter is at rest and moving, respectively. They simulated several different cases: no PCM with natural convection of air between cells, PCM, and PCM with embedded aluminum foam. The simulations are simply three discharge cycles, each followed by a long rest period to allow the batteries to cool to their initial temperature (30°C) through natural convection [$5\text{ W/(m}^2\text{ K)}$]. Although not specified, the batteries appear to be discharged at the $C/1$ rate (12 A) while the scooter is moving [$20\text{ W/(m}^2\text{ K)}$ applied convection coefficient]. Without PCM, the temperature rise of the battery is substantial: 35°C , with a 20°C temperature difference between the center and edge batteries. For the PCM-only simulations, the center cells experience a larger temperature rise than the edge cells. For example, the center cell temperature rises by 26.25 – 30°C , while the edge cells rise only by 18.75 – 22.5°C (exact values not specified). This is because the PCM has a poor thermal conductivity, and hence, it does not melt uniformly. The PCM near the center cells is completely melted during the first discharge cycle. Hence, solidification of the PCM causes the cell to remain at $\sim 10^{\circ}\text{C}$ above ambient during the rest period. However, the PCM near the cells by the cooled walls does not melt until the third cycle.

To reduce the temperature gradient inside the battery pack, they propose inserting an expanded metal foam matrix inside the PCM. This increases the effective thermal conductivity to 3 W/(m K) . As

a result, heat generated in the internal cells is more effectively transferred to the PCM near the outer cells. This allows the temperature rise to be within 1°C throughout discharge and the rest period. The PCM completely melts during discharge, but, due to the low thermal resistance on the surface of the battery, the PCM remains in the mushy phase by the end of the first discharge cycle. This causes the cells to start 8°C higher at the beginning of the second discharge cycle. To prevent this, they propose adding aluminum fins onto the sides of the battery case. Although the dimensions of these fins are not provided, they showed that the reduced thermal resistance from the external fins causes the PCM to not completely melt on discharge. Thus, the PCM solidifies and cools to the ambient temperature during the rest period, allowing each discharge cycle to start from the same temperature.

In a subsequent study, Sabbah et al.¹¹⁰ simulated and compared PCM and direct forced-air cooling of a large lithium-ion battery pack intended for HEV applications. The pack consists of 68 modules, with each module having a nominal voltage and capacity of 14.4 V and 7.5 Ah. Hence, the total available energy for the pack is 7.34 kWh. For forced-air cooling, it appears that the air cools each module in series fashion. The PCM composite has a density and specific heat of 866 kg/m³ and 1980 J/(kg K), respectively, and melts in the temperature range of 52–55°C with a latent heat of 181 kJ/kg. A graphite matrix is inserted into the PCM to improve the thermal conductivity, which is estimated at 16.6 W/(m K). It appears that the heat generated by the cells is rejected only to the PCM or the air in direct contact with the batteries. They simulated both a 2C and a 6.67C discharge for 25 and 45°C ambient/initial temperatures. Their results show little difference in the volume-averaged cell temperature (i.e., averaged across the entire pack, including the battery internals) between the two cooling strategies for a 25°C ambient temperature. For the PCM and increased convection ($Re = 637$), the average temperature rises by 8.1 and 17.9°C for the 2C and 6.67C discharge rates, respectively. However, there is a significant difference in the pack temperature gradient. For direct air cooling, the temperature gradients are approximately 2 and 4°C for 2C and 6.67C discharge, respectively, while they are only 0.03 and 0.07°C for the PCM. Similar results are obtained for the low rate discharge at 45°C. However, for the high rate discharge, the PCM begins to melt substantially; thus, its temperature rise is only 10°C with a temperature gradient less than 0.5°C. In contrast, the temperature of the directly air-cooled batteries rose by more than 15°C, with temperature gradients approaching 5°C. They also noted that increased surface convection increased the thermal gradient.

Although it effectively minimizes the thermal gradient inside the battery pack, the PCM concept has some disadvantages. For example, the PCM increases the volume and weight of the overall battery pack. In the design by Khateeb et al.,¹⁰⁹ the weight and volume of the cells in each module are 746 g and 297 cm³, while the combined weight and volume of the PCM/metal matrix are 466 g and 237 cm³. Furthermore, complete melting of the PCM matrix is possible during multiple charge/discharge cycles. If the PCM completely melts, the low thermal conductivity of even the PCM/metal matrix [3 W/(m K) for Khateeb et al.¹⁰⁹ and 16 W/(m K) for Sabbah et al.¹¹⁰] creates an additional large thermal resistance between the cooling fluid and the batteries, thus causing the battery temperatures to rise further, i.e., resulting in a worse situation than direct air cooling. Finally, because the melting range is tuned for cooling the batteries, warming in cold environments is difficult, and, due to the low thermal conductivity of the PCM/metal matrix, a temperature gradient among the cells would be established if externally warmed.

In all the above strategies, the thermal management system is external to the batteries. Because of the low thermal conductivity of the battery, heat builds up and the battery temperature rises. As an alternative, internal cooling of the batteries can be considered. This allows heat to be removed directly from the source without having to be rejected through the surface of the battery. Parise¹¹¹ proposed

integrating thermoelectric coolers into the assembly of plate-type lead–acid batteries. In addition, Choi and Yao¹¹² showed that forced circulation of the electrolyte in lead–acid batteries can lead to improved heat removal and cell temperature uniformity. Although the latter is not practical in lithium-ion batteries due to the high reactivity of lithium, internal cooling strategies for lithium-ion batteries should be explored further due to the potential for more uniform cooling both within an individual cell and among many cells within a pack. In addition, internal cooling strategies can dramatically increase the cooling surface area, which may be able to significantly reduce the effective thermal resistance between the heat generation locations and the cooling fluid. This should reduce the temperature rise for the batteries and allow the pack to withstand abusive thermal events. In addition, this may also limit SOC maldistribution created by temperature-induced current maldistribution.¹¹³

Summary and Conclusions

Lithium-ion battery performance characteristics are sensitive to the cell operating temperature. The recoverable power and capacity can be reduced significantly when these batteries are operated or stored at temperatures above ~50°C, especially at high SOC, due to multiple factors, including lithium loss from increased growth of the SEI on the negative electrode from it reacting with the electrolyte. This also leads to increases in ohmic resistances that reduce the deliverable power. The capacity may also be reduced if it is cycled at temperatures significantly below –10°C, which coincides with significant lithium plating on charging. At these low temperatures, the extractable energy is significantly reduced. Hence, it is imperative that lithium-ion batteries used in EV and HEV applications should be held at temperatures below 50°C but rapidly heated (or self-heated through cycling between acceptable limits) prior to operating at cold temperatures.

Electrical balancing among multiple lithium batteries in a single pack is critical for retrieving maximum energy and reducing the chance of overdischarging or overcharging individual cells. If temperature gradients exist among cells, the hotter cells will be capable of discharging or charging faster than the colder cells. Hence, electrical and temperature balances are linked together. The thermal management strategies that can more uniformly cool the batteries may have a positive impact on the electrical balance among the cells, perhaps allowing for less sophisticated electrical balancing schemes.

Perhaps the single limiting issue for lithium-ion batteries is safety. Lithium-ion batteries are very sensitive to overcharge, and, at temperatures near 100°C, deleterious heat-producing side reactions inside the battery can lead to even further increases in the battery temperature. Internal short circuiting can lead to rapid temperature rises in an individual cell, and the temperature increase in one cell can propagate to other nearby cells, thus causing them to rapidly self-heat, too. Furthermore, the energy released from these reactions can be significant and dangerous.

Thermal management strategies can play a critical role in mitigating all these effects. The operating temperature can be tuned to balance short-term performance with a desired battery lifetime, and electrical balancing schemes may become simpler if temperature is maintained uniformly throughout the pack. Thermal management schemes and devices that mitigate or counteract a rapid temperature rise triggered by thermal runaway would certainly improve the safety of large high energy packs.

Heat generation inside batteries arise from irreversibilities inside the battery and heat produced from the electrochemical reactions. As pointed out by multiple researchers, the development of concentration gradients also leads to the production of heat due to the temperature and concentration dependence of cell enthalpy, although this effect may be small in well designed batteries. Although dependent on cell chemistry and manufacturer specified voltage limits, the local electrochemical heat generation rate is generally a strong function of the current and SOC, with dramatic increases in the heat rate near the end of discharge and charge for low and high SOC, re-

spectively. In addition, large batteries required for HEV applications may have significant resistive heating in the current collectors due to long distances from the current source to the collection tab and increased current concentration near the tabs, even in batteries with well distributed current production.

There have been many experimental investigations that measure heat produced by lithium-ion batteries, but the overwhelming majority has been on small coin cells discharged/charged at low to moderate rates at near-ambient temperatures. Very few investigators have directly measured heat rates for lithium-ion batteries at rates above $C/1$, which routinely occur in HEV applications. Furthermore, of the studies conducted on geometrically and chemically similar cells, the results have been inconsistent. In some cases, for discharge beginning at the fully charged condition, the heat rate begins at 0 W/L, while others show a step-change to a nonzero value. Some studies also show an approximately linear increase in heat generation as discharge proceeds, while others show it roughly constant until the end of discharge is reached. The same cells tested using different methods also show significantly different results. These issues arise from difficulty in distinguishing the heat generation rate from heat storage inside the cell and have led to poor prediction of the temperature and volumetric heat generation rate at high currents. They also may be a consequence of significant variation of the heat generation rate due to different battery designs.

Thermal simulation studies have provided some important insights into the operation of lithium-ion batteries. As the temperature of the battery increases, the electrochemical efficiency of the battery improves, thus lowering its heat generation. In contrast, very few experimental studies have collected temperature-dependent data and those that have are restricted to narrow temperature and current ranges. The temperature dependence of heat generation causes the performance of the battery to be strongly dependent on thermal management. As demonstrated by the thermal simulations studies, the temperature gradient within an individual cell increases with improved surface convection. This temperature gradient causes portions of the cell to generate more current, which causes these hotter sections to increase further in temperature. This positive current-temperature feedback is countered by colder cells having increased polarization and thus higher heat generation. However, very few investigations have looked at the impacts of the cell-to-cell temperature balance within packs and the impact of temperature on the current distribution within a single battery. Furthermore, these studies have not accounted for the imbalance in the SOC caused by a current maldistribution, although some investigations at NREL are underway.^{52,53} This effect is important to characterize because imbalance in the SOC and temperature can lead to localized corrosion inside the battery.

The experimental results show that the entropic heat is nearly the same order of magnitude as the irreversible heat for the 1C discharge rate, thus having a nonnegligible impact on the heat generation and performance of a cell. However, the thermal simulation studies have not consistently modeled their effects. In some cases, the entropic heat coefficient is neglected or assumed constant, while others use complex functions describing the experimental data. Because heat accumulation throughout multiple cycles is important for HEV applications, entropic heat production should be included.

The essential thermal problem for batteries is the poor thermal conductivity that creates a large thermal resistance between the heat generation locations and the cooling fluid. This effect is even more pronounced for multicell battery packs. Air is the most common fluid used to cool battery packs, but, as demonstrated above, air cooling may not be the best method for maintaining cell temperature uniformity. Liquid cooling and PCM cooling can improve the cell-to-cell temperature uniformity. However, the PCM increases the thermal resistance between the battery and the cooling fluid, which causes the pack temperature to rise significantly, and the melting point is tuned to provide only cooling. Thus, rapid heating of cold batteries in PCM using an external fluid is not feasible. Some internal cooling techniques that reduce the inherent thermal resistance

between source and sink have been proposed, but more investigation is needed. Furthermore, although reported in the literature, the composite thermal conductivity of these batteries is not well known, especially perpendicular to the stack direction. This is a critical parameter for designing an effective thermal management system.

The previous investigations reviewed here lead to some important implications on thermal management systems used by lithium-ion battery packs for HEV applications. To mitigate self-discharge and power/capacity fade, batteries must be cooled to nominal ambient temperatures or lower (i.e., 20°C) in operation and during storage. If shown to dramatically prolong the life of the battery, the thermal management system could be coupled to a refrigeration system to chill the batteries below high ambient temperatures. In cold temperature environments, the batteries must be heated rapidly to improve both cycle life and energy extraction. Furthermore, due to its low density and specific heat, direct cooling with air is not the best method for evenly cooling large battery packs. This was clearly demonstrated in the commercial vehicle battery-pack tests, which show that even temperature distribution for air cooling was not easily achieved even when special air-baffling techniques were used. To minimize thermal gradients inside individual batteries and thermal energy accumulation, internal cooling strategies should be explored. The increased surface area from these solutions could mitigate the temperature distribution and rise inside the battery, which should allow for more uniform discharging and charging and less thermal accumulation from cycling by reducing the thermal resistance between the heat generation locations and the cooling media. Finally, the thermal management strategies for lithium-ion batteries should be capable of high heat removal during abuse events that cause localized heating. This would prevent the cascading temperature increases from cell to cell and make these large battery packs safer to implement.

Some areas of research in lithium-battery thermal issues need further exploration. First, it is evident that a thermal management technique that incorporates the above features does not exist. New techniques should be explored that allow for cold storage to limit capacity fade, fast heating to improve performance, even cooling to reduce complexity in electrical balancing schemes and increasing the amount of energy extracted, and fast cooling during critical heating events while minimizing auxiliary power consumption. In addition, there needs to be an experimental verification of the predicted heat generation rates and temperature distribution for high rate discharge and charge. Thermal modeling should also incorporate both life modeling and current/temperature feedback affecting SOC distribution, which has only begun to be investigated in lithium-ion batteries.¹¹⁴ These models should also be extended to entire packs such that the impact of thermal accumulation from continuous cycling in HEV applications can be fully understood. Along with a better understanding of the composite thermal conductivity of actual batteries, this would allow for more complete understanding of the impact of thermal management on battery pack performance.

Acknowledgment

The authors gratefully acknowledge support from Sandia National Laboratories in the form of the Excellence in Engineering Graduate Research Program fellowship for Todd M. Bandhauer.

List of Symbols

a	surface area per unit volume of porous electrode, m^{-1}
A	surface area, m^2
A_c	cross-sectional area, m^2
A_o	electrolyte conductivity constant multiplier, S/m
c	salt concentration in the electrolyte, mol/m^3
$c_{i,j}$	concentration of species i in phase j , mol/m^3
c_{Li}	concentration of lithium in the solid insertion electrode, mol/m^3
C_p	specific heat, $\text{J}/(\text{kg K})$
ΔH_s	enthalpy change per unit separator area, $\text{J}/(\text{mol m}^2)$
ΔH_o	enthalpy of activation at zero polarization, J/mol
ΔH_{rxn}	heat of reaction for anode decomposition, J

$\Delta H_{i,j \rightarrow m}^0$	molar enthalpy phase change of species i from phase j to m , J/mol
D_{Li}	diffusion coefficient of lithium in an insertion electrode, m^2/s
E_A	activation energy, J/mol
F	Faraday's constant, 96,487 C/equiv
h	heat transfer coefficient, $W/(m^2 K)$
\bar{H}_{Li}	partial molar enthalpy of lithium, J/mol
i	current density, A/m^2
i'''	current per unit cell volume, A/m^3
I	total cell current, A
i_n	interfacial current density, A/m^2
i_0	exchange current density, A/m^2
k	thermal conductivity, $W/(m K)$
k_i	thermal conductivity of each individual component in battery unit cell, $W/(m K)$
L	thickness of cell stack, m
M	mass, kg
N	number of cells per unit stack thickness, m^{-1}
$n_{i,j}$	moles of species i in phase j , mol
N_L	Lorentz number, $W/(S K^2)$
q	heat generation rate, W
q''	heat generation rate per unit separator area, W/m^2
q'''	heat generation rate per unit cell volume, W/m^3
R	universal gas constant, 8.314 J/(mol K)
R_t	electrical contact resistance between current collectors and electrodes, Ωm^2
$Rate_{rxn}$	rate of reaction for anode decomposition, s^{-1}
$(\rho C_p)_i$	heat capacity of each individual component in battery unit cell, $J/(m^3 K)$
$R_{particle}$	radius of particle, m
t	time, s
T	temperature, K
t_i	thickness of each individual component in battery unit cell, m
U	open circuit potential, V
U_H	enthalpy potential, V
v	volume, m^3
V	overall cell potential, V
V_{stack}	overall stack voltage, V
x_1	stack thickness position at front of porous electrode, m
x_2	stack thickness position at back of porous electrode, m

Greek

η	overpotential, V
$\gamma_{i,j}$	activity coefficient of species i in phase j
∞	bulk property or volume average value
ϕ	local potential in stack, V
ρ	density, kg/m^3
σ	electrical conductivity, S/m
σ_{SB}	Stefan-Boltzmann constant, $5.67 \times 10^{-8} W/(m^2 K^4)$
ϵ	volume fraction or emissivity

Subscripts or Superscripts

a	anode (negative electrode)
avg	average
c	cathode (positive electrode)
cc	current collector
cha	charge
dis	discharge
e	electrolyte
ent	entropic or reversible
env	environment
heater	external source heater
i	species index
insertion	insertion electrode
j	phase index
l	reaction number index
Li	inserted lithium
m	phase index
neg	negative electrode
pos	positive electrode
s	separator
surf	surface
well	calorimeter well temperature
wire	copper lead wire
x	cell thickness direction
1	solid phase
2	electrolyte phase
	parallel to wound stack direction
⊥	perpendicular to wound stack direction

References

- D. Linden, in *Handbook of Batteries*, 3rd ed., D. Linden and T. B. Reddy, Editors, p. 1.3, McGraw-Hill, New York (2002).
- F. V. Conte, *Elektrotechnik Informationstechnik*, **123**, 424 (2006).
- S. R. Alavi-Soltani, T. S. Ravigururajan, and M. Rezac, in *Proceedings of IMECE 2006*, American Society of Mechanical Engineers, p. 383 (2006).
- P. Nelson, D. Dees, K. Amine, and G. Henriksen, *J. Power Sources*, **110**, 349 (2002).
- FreedomCAR Battery Test Manual*, Revision 3. DOE/ID-11069 (2003).
- E. V. Thomas, H. L. Case, D. H. Doughty, R. G. Jungst, G. Nagasubramanian, and E. P. Roth, *J. Power Sources*, **124**, 254 (2003).
- M. Broussely, in *Advances in Lithium-Ion Batteries*, W. A. V. Schalkwijk and B. Scrosati, Editors, p. 393, Kluwer Academic/Plenum Publishers, New York (2002).
- P. Arora, R. E. White, and M. Doyle, *J. Electrochem. Soc.*, **145**, 3647 (1998).
- D. Aurbach, B. Markovsky, G. Salitra, E. Markevich, Y. Talyossef, M. Koltypin, L. Nazar, B. Ellis, and D. Kovacheva, *J. Power Sources*, **165**, 491 (2007).
- M. Broussely, P. Biensan, F. Bonhomme, P. Blanchard, S. Herreyre, K. Nechev, and R. J. Staniewicz, *J. Power Sources*, **146**, 90 (2005).
- J. Vetter, P. Novák, M. R. Wagner, C. Veit, K. C. Möller, J. O. Besenhard, M. Winter, M. Wohlfahrt-Mehrens, C. Vogler, and A. Hammouche, *J. Power Sources*, **147**, 269 (2005).
- P. Ramadass, B. Haran, R. White, and B. N. Popov, *J. Power Sources*, **112**, 606 (2002).
- P. Ramadass, B. Haran, R. White, and B. N. Popov, *J. Power Sources*, **112**, 614 (2002).
- G. M. Ehrlich, in *Handbook of Batteries*, 3rd ed., D. Linden and T. B. Reddy, Editors, p. 35.1, McGraw-Hill, New York (2002).
- K. Amine, J. Liu, and I. Belharouak, *Electrochem. Commun.*, **7**, 669 (2005).
- P. Liu, J. Wang, J. Hicks-Garner, E. Sherman, S. Soukiazian, M. Verbrugge, H. Tataria, J. Musser, and P. Finamore, *J. Electrochem. Soc.*, **157**, A499 (2010).
- K. Takei, K. Kumai, Y. Kobayashi, H. Miyashiro, N. Terada, T. Iwahori, and T. Tanaka, *J. Power Sources*, **97-98**, 697 (2001).
- S. S. Choi and H. S. Lim, *J. Power Sources*, **111**, 130 (2002).
- J. R. Belt, C. D. Ho, C. G. Motloch, T. J. Miller, and T. Q. Duong, *J. Power Sources*, **123**, 241 (2003).
- J. R. Belt, C. D. Ho, T. J. Miller, M. A. Habib, and T. Q. Duong, *J. Power Sources*, **142**, 354 (2005).
- M. C. Smart, B. V. Ratnakumar, J. Whitacre, L. Whitcanack, K. Chin, M. Rodriguez, and S. Surampudi, in *Battery Conference on Applications and Advances, 2002. The Seventeenth Annual*, Institute of Electrical and Electronics Engineers, p. 53 (2002).
- D. Aurbach, *J. Power Sources*, **146**, 71 (2005).
- B. A. Johnson and R. E. White, *J. Power Sources*, **70**, 48 (1998).
- R. Spotnitz and J. Franklin, *J. Power Sources*, **113**, 81 (2003).
- D. P. Abraham, E. P. Roth, R. Kostecki, K. McCarthy, S. MacLaren, and D. H. Doughty, *J. Power Sources*, **161**, 648 (2006).
- H. Joachin, T. D. Kaun, K. Zaghib, and J. Prakash, *J. Electrochem. Soc.*, **156**, A401 (2009).
- H. Yang, S. Amiruddin, H. J. Bang, Y. K. Sun, and J. Prakash, *J. Ind. Eng. Chem. (Seoul, Repub. Korea)*, **12**, 12 (2006).
- S. Al Hallaj, H. Maleki, J. S. Hong, and J. R. Selman, *J. Power Sources*, **83**, 1 (1999).
- M. W. Verbrugge, *AIChE J.*, **41**, 1550 (1995).
- Y. Chen and J. W. Evans, *J. Electrochem. Soc.*, **143**, 2708 (1996).
- G.-H. Kim, A. Pesaran, and R. Spotnitz, *J. Power Sources*, **170**, 476 (2007).
- E. P. Roth, D. H. Doughty, and J. Franklin, *J. Power Sources*, **134**, 222 (2004).
- P. G. Balakrishnan, R. Ramesh, and T. Prem Kumar, *J. Power Sources*, **155**, 401 (2006).
- L. Song and J. W. Evans, *J. Electrochem. Soc.*, **145**, 2327 (1998).
- J. R. Dahn, E. W. Fuller, M. Obrovac, and U. von Sacken, *Solid State Ionics*, **69**, 265 (1994).
- B. E. Dickinson and D. H. Swan, in *Future Transportation Technology Conference & Exposition*, Technical report 951949, Society of Automotive Engineers (1995).
- B. T. Kuhn, G. E. Pitel, and P. T. Krein, in *Vehicle Power and Propulsion, 2005 IEEE Conference*, G. E. Pitel, Editor, IEEE, p. 5 (2005).
- S. W. Moore and P. J. Schnieder, in *SAE 2001 World Congress*, Society of Automotive Engineers, Detroit, MI (2001).
- A. Vlahinos and A. Pesaran, in *2002 SAE Future Car Congress*, Computer Optical Disc, Crystal City, Arlington, VA, p. 1 (2002).
- M. D. Zolot, K. Kelly, M. Keyser, M. Mihalic, A. Pesaran, and A. Hieronymus, in *36th Intersociety Energy Conversion Engineering Conference*, American Society of Mechanical Engineers, p. 923 (2001).
- S. S. Zhang, K. Xu, and T. R. Jow, *J. Power Sources*, **115**, 137 (2003).
- J. Fan and S. Tan, *J. Electrochem. Soc.*, **153**, A1081 (2006).
- G. Nagasubramanian, *J. Appl. Electrochem.*, **31**, 99 (2001).
- S. S. Zhang, K. Xu, and T. R. Jow, *J. Solid State Electrochem.*, **7**, 147 (2003).
- D. Bernardi, E. Pawlikowski, and J. Newman, *J. Electrochem. Soc.*, **132**, 5 (1985).
- W. B. Gu and C. Y. Wang, *J. Electrochem. Soc.*, **147**, 2910 (2000).
- J. M. Sherfey and A. Brenner, *J. Electrochem. Soc.*, **105**, 665 (1958).
- L. Rao and J. Newman, *J. Electrochem. Soc.*, **144**, 2697 (1997).
- K. E. Thomas and J. Newman, *J. Electrochem. Soc.*, **150**, A176 (2003).
- U. S. Kim, C. B. Shin, and C.-S. Kim, *J. Power Sources*, **180**, 909 (2008).
- U. S. Kim, C. B. Shin, and C.-S. Kim, *J. Power Sources*, **189**, 841 (2009).
- G.-H. Kim and K. Smith, Abstract 1295, The Electrochemical Society Meeting Abstracts, Vol. 802, Honolulu, HI, Oct 12-17, 2008.
- G.-H. Kim and K. A. Smith, Abstract 252, The Electrochemical Society Meeting

- Abstracts, Vol. 901, San Francisco, CA, May 24–29, 2009.
54. S. Al Hallaj, R. Venkatachalapathy, J. Prakash, and J. R. Selman, *J. Electrochem. Soc.*, **147**, 2432 (2000).
55. S. Al Hallaj, J. Prakash, and J. R. Selman, *J. Power Sources*, **87**, 186 (2000).
56. J. S. Hong, H. Maleki, S. A. Hallaj, L. Redey, and J. R. Selman, *J. Electrochem. Soc.*, **145**, 1489 (1998).
57. H. Bang, H. Yang, Y. K. Sun, and J. Prakash, *J. Electrochem. Soc.*, **152**, A421 (2005).
58. J.-S. Kim, J. Prakash, and J. R. Selman, *Electrochem. Solid-State Lett.*, **4**, A141 (2001).
59. Y. Kobayashi, N. Kihira, K. Takei, H. Miyashiro, K. Kumai, N. Terada, and R. Ishikawa, *J. Power Sources*, **81–82**, 463 (1999).
60. Y. Kobayashi, H. Miyashiro, K. Kumai, K. Takei, T. Iwahori, and I. Uchida, *J. Electrochem. Soc.*, **149**, A978 (2002).
61. W. Lu and J. Prakash, *J. Electrochem. Soc.*, **150**, A262 (2003).
62. W. Lu, I. Belharouak, D. Vissers, and K. Amine, *J. Electrochem. Soc.*, **153**, A2147 (2006).
63. W. Lu, H. Yang, and J. Prakash, *Electrochim. Acta*, **51**, 1322 (2006).
64. W. Lu, I. Belharouak, S. H. Park, Y. K. Sun, and K. Amine, *Electrochim. Acta*, **52**, 5837 (2007).
65. K. Onda, H. Kameyama, T. Hanamoto, and K. Ito, *J. Electrochem. Soc.*, **150**, A285 (2003).
66. Y. Saito, K. Kanari, and K. Takano, *J. Power Sources*, **68**, 451 (1997).
67. Y. Saito, K. Takano, K. Kanari, A. Negishi, K. Nozaki, and K. Kato, *J. Power Sources*, **97–98**, 688 (2001).
68. L. Song and J. W. Evans, *J. Electrochem. Soc.*, **147**, 2086 (2000).
69. H. Yang and J. Prakash, *J. Electrochem. Soc.*, **151**, A1222 (2004).
70. H. Vaidyanathan, W. H. Kelly, and G. Rao, *J. Power Sources*, **93**, 112 (2001).
71. K. Onda, T. Ohshima, M. Nakayama, K. Fukuda, and T. Araki, *J. Power Sources*, **158**, 535 (2006).
72. K. E. Thomas and J. Newman, *J. Power Sources*, **119–121**, 844 (2003).
73. K. E. Thomas, C. Bogatu, and J. Newman, *J. Electrochem. Soc.*, **148**, A570 (2001).
74. J. N. Reimers and J. R. Dahn, *J. Electrochem. Soc.*, **139**, 2091 (1992).
75. V. V. Viswanathan, D. Choi, D. Wang, W. Xu, S. Towne, R. E. Williford, J.-G. Zhang, J. Liu, and Z. Yang, *J. Power Sources*, **195**, 3720 (2010).
76. C. R. Pals and J. Newman, *J. Electrochem. Soc.*, **142**, 3282 (1995).
77. G. G. Botte, B. A. Johnson, and R. E. White, *J. Electrochem. Soc.*, **146**, 914 (1999).
78. V. Srinivasan and C. Y. Wang, *J. Electrochem. Soc.*, **150**, A98 (2003).
79. K. Smith and C. Y. Wang, *J. Power Sources*, **160**, 662 (2006).
80. K. Smith, Personal communication.
81. P. M. Gomadam, J. W. Weidner, R. A. Dougal, and R. E. White, *J. Power Sources*, **110**, 267 (2002).
82. K. Kumaresan, G. Sikha, and R. E. White, *J. Electrochem. Soc.*, **155**, A164 (2008).
83. C. R. Pals and J. Newman, *J. Electrochem. Soc.*, **142**, 3274 (1995).
84. S.-C. Chen, Y.-Y. Wang, and C.-C. Wan, *J. Electrochem. Soc.*, **153**, A637 (2006).
85. Y. Chen and J. W. Evans, *J. Electrochem. Soc.*, **140**, 1833 (1993).
86. Y. Chen and J. W. Evans, *Electrochim. Acta*, **39**, 517 (1994).
87. Y. Chen and J. W. Evans, *J. Electrochem. Soc.*, **141**, 2947 (1994).
88. S. C. Chen, C. C. Wan, and Y. Y. Wang, *J. Power Sources*, **140**, 111 (2005).
89. A. Hooper and J. M. North, *Solid State Ionics*, **9–10**, 1161 (1983).
90. M. Gauthier, D. Fauteux, G. Vassort, A. Belanger, M. Duval, P. Ricoux, J. M. Chabagno, D. Muller, P. Rigaud, M. B. Armand, and D. Deroo, *J. Electrochem. Soc.*, **132**, 1333 (1985).
91. G. Au and M. Sulkes, *Performance of the Sony Lithium-Ion Rechargeable Battery*, p. 37, Report no. ARL-TR-71, U.S. Army Research Laboratory (1993).
92. T. F. Fuller, M. Doyle, and J. Newman, *J. Electrochem. Soc.*, **141**, 1 (1994).
93. M. Doyle, T. F. Fuller, and J. Newman, *J. Electrochem. Soc.*, **140**, 1526 (1993).
94. J. R. Dahn, U. von Sacken, M. W. Jozkew, and H. Al-Janaby, *J. Electrochem. Soc.*, **138**, 2207 (1991).
95. M. Doyle, *Chemical Engineering*, p. 1890, University of California–Berkeley, Berkeley, CA (1995).
96. M. Doyle, J. Newman, A. S. Gozdz, C. N. Schmutz, and J. M. Tarascon, *J. Electrochem. Soc.*, **143**, 1890 (1996).
97. J. S. Newman and K. E. Thomas-Alyea, *Electrochemical systems*, 3rd ed., p. 517, John Wiley & Sons, Hoboken, NJ (2004).
98. H. Maleki, S. Al Hallaj, J. R. Selman, R. B. Dinwiddie, and H. Wang, *J. Electrochem. Soc.*, **146**, 947 (1999).
99. G. W. Gokel and J. A. Dean, *Dean's Handbook of Organic Chemistry*, p. 1 v. (various pagings), McGraw-Hill, New York (2004).
100. X. Jin, J. Wu, Z. Liu, and J. Pan, *Fluid Phase Equilib.*, **220**, 37 (2004).
101. G. Guo, B. Long, B. Cheng, S. Zhou, P. Xu, and B. Cao, *J. Power Sources*, **195**, 2393 (2010).
102. S.-Y. Chung, J. T. Bloking, and Y.-M. Chiang, *Nature Mater.*, **1**, 123 (2002).
103. K. J. Kelly, M. Mihalic, and M. Zolot, in *17th Annual Battery Conference on Applications and Advances*, Institute of Electrical and Electronics Engineers, p. 247 (2002).
104. M. Zolot, A. A. Pesaran, and M. Mihalic, in *Future Car Congress*, 2002–01–1962, Society of Automotive Engineers (2002).
105. A. Zhukauskas, in *Advances in Heat Transfer*, J. P. Hartnett and T. F. Irvine Editors, Academic, New York (1972).
106. F. P. Incropera and D. P. DeWitt, *Fundamentals of Heat and Mass Transfer*, 4th ed., p. xxiii, John Wiley & Sons, New York (1996).
107. S. Al Hallaj and J. R. Selman, *J. Electrochem. Soc.*, **147**, 3231 (2000).
108. S. A. Khateeb, S. Amiruddin, M. Farid, J. R. Selman, and S. Al-Hallaj, *J. Power Sources*, **142**, 345 (2005).
109. S. A. Khateeb, M. M. Farid, J. R. Selman, and S. Al-Hallaj, *J. Power Sources*, **128**, 292 (2004).
110. R. Sabbah, R. Kizilel, J. R. Selman, and S. Al-Hallaj, *J. Power Sources*, **182**, 630 (2008).
111. R. J. Parise, in *Energy Conversion Engineering Conference and Exhibit, 2000*. (IECEC) 35th Intersociety, p. 120 (2000).
112. K. W. Choi and N. P. Yao, *J. Electrochem. Soc.*, **126**, 1321 (1979).
113. T. M. Bandhauer, S. Garimella, and T. F. Fuller, Abstract 553, The Electrochemical Society Meeting Abstracts, Vol. 802, Honolulu, HI, Oct 12–17, 2008.
114. K. A. Smith and G.-H. Kim, Abstract 255, The Electrochemical Society Meeting Abstracts, Vol. 901, San Francisco, CA, May 24–29, 2009.